



Contents lists available at ScienceDirect

International Journal of Plasticity

journal homepage: www.elsevier.com/locate/ijplas



Role of layer thickness and dislocation distribution in confined layer slip in nanolaminated Nb

Wu-Rong Jian ^{a,*}, Shuzhi Xu ^a, Yanqing Su ^b, Irene J. Beyerlein ^{a,c}

^a Department of Mechanical Engineering, University of California, Santa Barbara, CA 93106-5070, USA

^b Department of Mechanical and Aerospace Engineering, Utah State University, Logan, UT 84322-4130, USA

^c Materials Department, University of California, Santa Barbara, CA 93106-5050, USA



ARTICLE INFO

Keywords:

Confined layer slip
Nanolaminates
Layer thickness
Dislocation distribution
Atomistic simulations

ABSTRACT

Confined layer slip (CLS) is considered as the primary mechanism for plastic deformation in nanolaminates. It depicts the confined motion of a single dislocation between two parallel interfaces nanometers apart. Using atomistic simulations, we investigate the effects of interface spacing, or equivalently individual layer thickness, and dislocation distribution on the CLS of an edge dislocation in nanolaminated Nb with coherent twin boundaries and Nb nanofilm. We show that CLS motion transitions from smooth glide to staggered glide as the nanolayer thickness increases, while the line bows out, as theoretically pictured. For the same nanolayer thicknesses L , dislocation CLS in the nanofilm is smooth and the CLS resistance is 47% to 79% lower. For both the nanolaminate and film, the nanolayer size L effect on CLS resistance is found to follow the expected $\ln(L)/L$ scaling with an additional constant that depends on the interface/dislocation interaction but is independent of L . When like-signed dislocation glide concurrently on the same glide plane in the adjacent layers, the dislocations move with almost no bow-out, and the CLS resistance is substantially reduced, even below that of the thin film bounded by two free surfaces. With an increase in the glide plane separation between like-signed dislocations in the neighboring layers, a higher flow stress is obtained. However, when the dislocations are oppositely signed, CLS motion is jerky and the stress fluctuates and overall increases three fold.

1. Introduction

In recent years, metal-based nanolaminates have been the focus of intense research, due to their excellent mechanical performance (Pathak et al., 2017; Nasim et al., 2020; Demkowicz and Beyerlein, 2020), e.g., high ductility (Misra et al., 2004), high strength (Yang et al., 2019), fatigue resistance (Wang et al., 2006), and the stability under irradiation (Zhang et al., 2012; Kashinath et al., 2013; Li et al., 2017; Wang et al., 2018a; Yang et al., 2019). Nanolaminates consist of alternating nanometer-scale layers, and among those studied, the layer compositions can be the same material, such as in nanotwinned Cu (Pan et al., 2017; Cheng et al., 2018) and nanotwinned Ag (Bufford et al., 2011), or different materials, such as in Cu/Ag (Wang et al., 2018a, 2020), Cu/Nb (Li et al., 2012a), Mg/Ti (Lu et al., 2014), and Zr/Nb (Frutos et al., 2015; Lin et al., 2020) bimetal nanolaminates. The layers in nanolaminates can be either single crystalline (Jang et al., 2012) or nanocrystalline layers (Bufford et al., 2011; Cheng et al., 2018; Zheng et al., 2012). In some cases, one phase in the composite may be a ceramic (Salehinia et al., 2014; Singh et al., 2010) or an amorphous metal (Wang et al., 2007), while the other phase is a crystalline metal. Their exceptional strengths and other

* Corresponding author.

E-mail address: wurong@ucsb.edu (W.-R. Jian).

mechanical properties are closely related to the dislocation-based deformation mechanisms occurring in the metal layer (Wang and Misra, 2011; Wang et al., 2017; Snel et al., 2017).

For the metal layers, many of these mechanisms and how they operate depend on the nanolayer thickness (Wang et al., 2017; Nasim et al., 2020). For large layer thicknesses, greater than 100 nm, the layer is sufficiently thick to allow dislocation pile-ups to form (Xu et al., 2016b, 2017, 2020a; Selimov et al., 2021). The strength/flow stress scales as $1/\sqrt{L}$, where L is the layer thickness (Tench and White, 1984; Parker, 1985). This relation follows the well known Hall-Petch law (Hall, 1951; Petch, 1953), which describes the increase in strength of polycrystalline materials with decrease in grain size. For intermediate layer thicknesses, i.e., 5 to 100 nm (Wang and Misra, 2011), dislocation glide becomes confined between two parallel interfaces under applied stress (Phillips et al., 2003). Such confined layer slip (CLS) by the dislocation has been related to nanolaminate strength (Nix, 1989; Freund, 1990; Embury and Hirth, 1994; Anderson et al., 1999; Misra et al., 2002). In the CLS theory, the strength scales with $\ln(L)/L$, unlike that of Hall-Petch, $1/\sqrt{L}$. In-situ transmission electron microscope (TEM) studies have directly confirmed CLS in both Cu and Nb layers within Cu/Nb nanolaminates with L of a few tens of nanometers (Li et al., 2012b). For extremely small L , generally less than 5 nm, the main mechanism becomes dislocation interface crossing (Misra et al., 1998; Callisti and Polcar, 2017). In this case, L is too thin for CLS and pile ups to be possible. The dislocation must be able to transmit across the interfaces to propagate (Misra et al., 2002; Hoagland et al., 2004; Derlet et al., 2009a). In this regime, nanolaminate strength becomes independent of L and determined by the interface barrier strength.

The typical range for L in most studied nanolaminates spans from 5 nm to 100 nm (Subedi et al., 2018), bringing the CLS model into focus. The original CLS theory stems from the analysis by Freund (1987) on the motion of threading dislocation in the strained layer on the substrate. Applying this analysis to a nanometer thin film sandwiched between an oxide layer and substrate, Nix (1989) derived the critical biaxial normal stress to propagate the threading dislocation as

$$\sigma_b = \frac{\sin \chi}{\cos \chi \cos \gamma} \frac{b}{2\pi(1-v)L} \left[\frac{G_f G_s}{(G_f + G_s)} \ln \left(\frac{\beta_s L}{b} \right) + \frac{G_f G_o}{(G_f + G_o)} \ln \left(\frac{\beta_o L_o}{b} \right) \right], \quad (1)$$

where χ and γ are the angles between film normal and the normal of the slip plane and the Burgers vector, respectively; b , v , G , and β are the Burgers vector magnitude, Poisson's ratio, shear modulus, and a numerical constant, respectively. Subscripts f, s, and o respectively denote the film, substrate, and oxide layers. Comparison between Eq. (1) and experimental results on a polycrystalline aluminum thin film between a Si substrate and oxide layer found that this formula underestimates strength. To better describe the measurement, Nix (1989) added a Hall-Petch term to Eq. (1) to account for the effect of grain size d_c :

$$\sigma_b = \frac{\sin \chi}{\cos \chi \cos \gamma} \frac{b}{2\pi(1-v)L} \left[\frac{G_f G_s}{(G_f + G_s)} \ln \left(\frac{\beta_s L}{b} \right) + \frac{G_f G_o}{(G_f + G_o)} \ln \left(\frac{\beta_o L_o}{b} \right) \right] + \frac{k}{\sqrt{d_c}}, \quad (2)$$

where k is a constant. Later, Embury and Hirth (1994) pointed out the stress to move a single dislocation within the lamella follows a Orowan-like relation, in which the dislocation bows out in the glide plane, while being held back at the dislocation/interface junctions. The increase in line tension associated with bowing results in resistance to dislocation motion, expressed as:

$$\tau = \frac{Gb}{\pi(1-v)L} \ln \left(\frac{h}{2\pi b} \right), \quad (3)$$

where h is a characteristic length. Applying it to CLS in bimetal nanolaminates, Misra et al. (2005) extended Nix's analysis (Eq. (1)) to obtain a CLS shear stress, given by

$$\tau = \frac{Gb \sin \chi}{8\pi L} \left(\frac{4-v}{1-v} \right) \ln \left(\frac{\alpha L}{b \sin \chi} \right), \quad (4)$$

where α denotes a core cutoff parameter, which is related to the radius of dislocation core, r_{core} , via $\alpha = b/r_{\text{core}}$ (Hirth and Lothe, 1982). χ takes on the same definition as in Eq. (1). The model was extended by Misra et al. (2005) to describe measured strengths of nanolaminates obtained from hardness tests applied normal to the layers.

To fit the experimental data well, the term involving the interface stress effect f/L was also added by Misra et al. (2005) and the CLS normal stress is modified as

$$\sigma = T \frac{Gb \sin \chi}{8\pi L} \left(\frac{4-v}{1-v} \right) \ln \left(\frac{\alpha L}{b \sin \chi} \right) - \frac{f}{L}. \quad (5)$$

For the first term, the critical shear stress in Eq. (4) is related to the normal stress σ by Taylor factor T . The second term is the interface stress effect f/L , where f is the change in interface energy with straining and has the same units as interface energy (J/m^2). The authors had also added a third term to Eq. (5) to reflect the resistance from the interfacial dislocations in the interface:

$$\sigma = T \frac{Gb \sin \chi}{8\pi L} \left(\frac{4-v}{1-v} \right) \ln \left(\frac{\alpha L}{b \sin \chi} \right) - \frac{f}{L} + \frac{Gb}{(1-v)\lambda}, \quad (6)$$

where λ is interfacial dislocation array spacing. Eq. (6) provided a good fit to the measured strengths of Cu/Nb nanolaminates down to a L of 2 nm. Recently, Subedi et al. (2018) proposed another form for the CLS normal stress based on the Hall-Petch equation

$$\sigma_{\text{HP}} = \sigma_0 + \frac{k}{\sqrt{L}}, \quad (7)$$

where σ_0 is the friction stress that is independent of grain size or L . This model was shown to also provide a suitable model for flow strength, down to L of 5 nm, for a broad variety of nanolaminate systems. The coefficient k traditionally has been related to the shear modulus G , dislocation Burgers vector b , and the resistance against slip transmission (Armstrong, 2014). Subedi et al. (2018) additionally related k to the density of interfacial dislocations, revising the strength σ_{HP} in Eq. (7) as

$$\sigma_{\text{HP}} = \beta G b \sqrt{\frac{\rho_{\text{int}}}{L}}, \quad (8)$$

where β is a constant and ρ_{int} denotes the density of interfacial dislocations.

While the resistances to dislocation motion proposed in the analytical models of Eqs. (6) and (7) have physical bases, they introduce fitting parameters that need to be characterized by matching to macroscopic hardness or strength data. They also differ in their scaling with L , with Eq. (6) proposing an additional interface-dependent second term that is inversely related to L and Eq. (7) inversely related to \sqrt{L} . Also, like most CLS models, they envision a single dislocation threading in one layer, while the adjacent layers are dislocation-free (Freund, 1987; Nix, 1989; Embury and Hirth, 1994; Misra et al., 2005; Phillips et al., 2003). However, as argued in (Phillips et al., 2003), it is possible that other dislocations could be simultaneously threading in the neighboring layers. The interactions between moving dislocations in adjacent layers could affect the resistance to CLS and, in turn, the strength of the material. The effects of dislocation distribution and interface structure, in addition to L , are difficult to isolate from macroscopic tests.

The main challenge is understanding how the CLS mechanism proceeds in time as layer thickness changes. Direct observation via in-situ TEM is possible but too challenging at present to repeat with different layer thicknesses. In analytical models, the mechanism is often presumed a priori making it difficult to understand when transitions in mechanisms occur. As a complement to experiments and theory, molecular dynamics (MD) simulation has been applied to investigate deformation mechanisms in nanolaminates at the atomic and nanoscales (Misra et al., 2008; Derlet et al., 2009b; Jian et al., 2018; Xie et al., 2020; Turlo and Rupert, 2018; Jian et al., 2021a). For CLS in nanolaminates, such simulations would be able to track the motion of dislocations, accounting for the interaction between the dislocation core and the atomic structure of the interface. Only a few MD studies to date, however, have simulated CLS (Turlo and Rupert, 2018; Jian et al., 2021a). Turlo and Rupert (2018) revealed that both ordered and disordered Cu-Zr grain boundary complexions can enhance the stress required for confined dislocation glide between two parallel 90° twist grain boundaries. They attributed the strengthening effect to the local ledges and stress variation at grain boundaries caused by Zr dopants. Recently, Jian et al. (2021a) conducted MD simulations to study the effect of interface structure on a single dislocation gliding in Cu/Nb, Nb/Cu, Cu/Cu, and Nb/Nb nanolaminates. They showed dislocation motion was jerky, i.e., stop and starting repeatedly, when gliding in the Cu layer in the Cu/Nb and Cu/Cu nanolaminates and in the Nb layer in the Cu/Nb nanolaminate due to the discrete misfit dislocation arrays within the incoherent interfaces, while it was smooth when gliding in the Nb layer in the Nb/Nb nanolaminate with coherent nanotwinned interfaces containing no original misfit dislocations. In particular, when a misfit dislocation in the Cu/Nb interface, partially extended a fault into the Cu crystal, the glide resistance increased several fold, since the dislocation had to transfer to another plane in order to circumvent the misfit dislocation and glide. These studies clearly demonstrated the importance of dislocation core/interface structure interactions at the atomic scale on the resistance to dislocation glide and hence strength. However, the related MD studies are still scarce.

In this work, using the MD method, we study the effect of layer thickness on the CLS of edge dislocations in a Nb/Nb nanotwinned nanolaminate and identify an appropriate scaling law. Selection of the nanotwinned structure was motivated by the occurrence of deformation twinning in plastically deformed Nb (Boucher and Christian, 1972; Wang et al., 2018b). This type of nanostructure serves as a model material that enables us to focus on the effect of layer size on dislocation glide. The coherent twin boundaries (CTBs) do not contain original misfit dislocations, which, as mentioned, have been shown to disrupt the CLS motion of dislocations (Jian et al., 2021a). In addition, the glide plane of the confined dislocation is perpendicular to the CTBs in nanotwinned Nb, and thus it is easy to build the model with periodic boundary conditions (PBCs) that allows the simulation of CLS for enough time. In body-centered cubic (BCC) Nb, the edge dislocations are compact and planar and not extended or spread (Xu et al., 2021; Jian et al., 2021b; Wang et al., 2021) as the same dislocations in some face-centered cubic materials (Xu et al., 2019c; Jian et al., 2020). These features best represent the idealized assumptions made in most analytical models to date. By contrast, the core of screw dislocation is not compact but non-planar, and thus, the screw dislocation may cross slip from the habit plane to another non-parallel plane, which makes the CLS simulation of screw dislocation much more complicated. Now, we only consider the CLS simulation of edge dislocation. The more complicated case of the screw dislocation is beyond the scope of this work and will be investigated in the future. To best highlight the role of the interface, we also repeat the calculations and size effect analysis on a nanofilm of the same thickness wherein the layer is bounded by free surfaces. We show that when $L > 40$ nm, dislocation CLS motion within the layers is jerky, in which each end alternately pins and depins from the interface. The effects of dislocations gliding in the neighboring layers are also examined. Neighboring like-signed dislocation that glide synchronously on the same planes substantially lower the CLS stress. Also, in this case, glide is smooth, and the layer size effect on CLS stress is weak. When CLS models are compared with the MD results for a Nb film and nanolaminate with and without neighboring dislocations, we find the interface-dislocation interaction can be captured by an additional layer thickness-independent interface resistance term. The dynamics and corresponding CLS stress of other dislocation distributions are also probed.

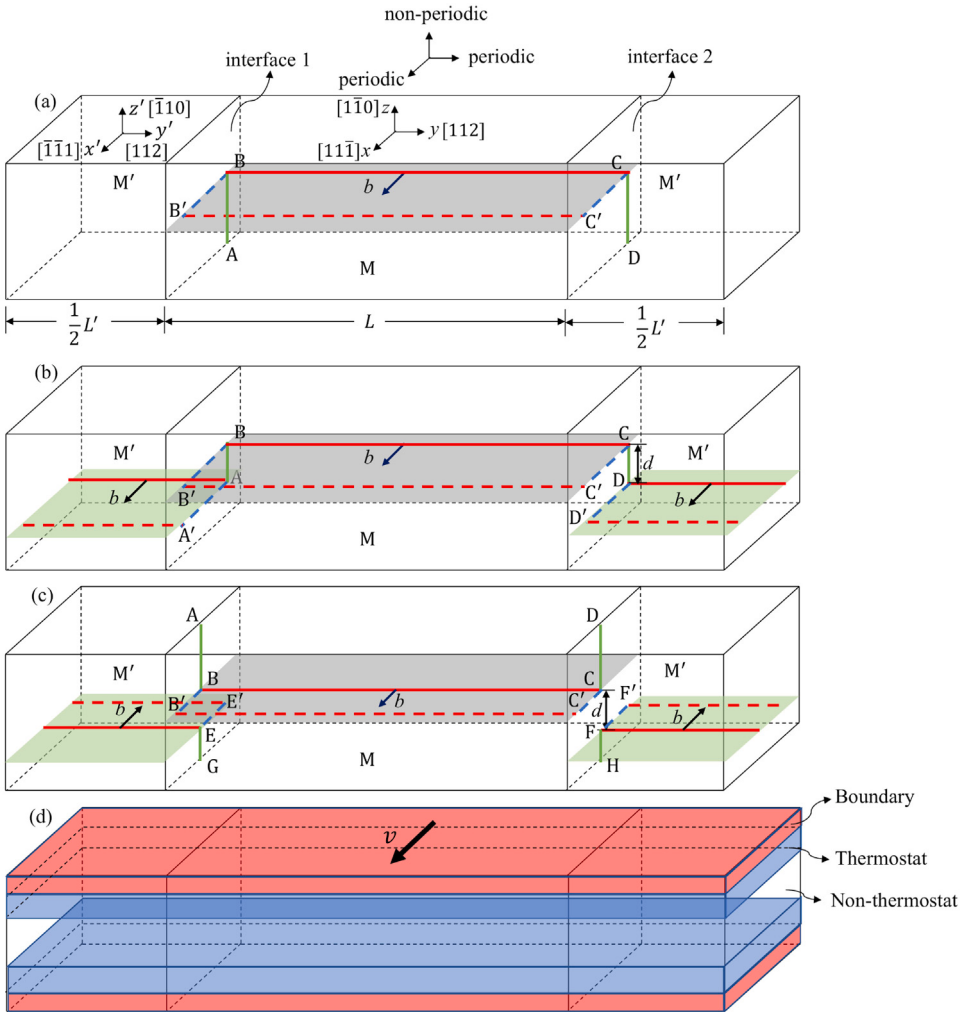


Fig. 1. Schematics of the atomic configuration used to simulate confined layer slip (CLS) in the Nb nanolaminate. The inserted edge dislocations with Burgers vector \mathbf{b} are represented by the red solid lines along y direction, while the green solid lines along z direction at the interfaces are the misfit edge dislocations created by inserting the confined edge dislocation to either layer M only or both layers. The red dashed lines denote the moving edge dislocations, each of which drags two misfit screw dislocations at the interfaces, as shown by the blue dashed lines. (a), (b) and (c) correspond to Alt-NL, All-NL-S and All-NL-O configurations. The spacing between the glide planes of the neighboring dislocations in M and M' layers is d in (b) and (c). As displayed in (d), the whole system is divided into colorless, blue and red regions during shear loading, corresponding to non-thermostat, thermostat and boundary regions, respectively. The arrow in (d) denotes the shear loading direction. (For interpretation of the references to color in this figure legend, the reader is referred to the web version of this article.)

2. Methodology

We carry out all MD simulations using LAMMPS (Plimpton, 1995). The Ackland and Thetford potential (Ackland and Thetford, 1987) was selected for the Nb interatomic potential describing the interactions between Nb atoms. The basic structural parameters (Jian et al., 2021b) and generalized stacking fault energies on $\{110\}$ (Xu et al., 2022) and $\{112\}$ (Jian et al., 2021b) planes predicted by this potential agree well with those from density functional theory calculations (Xu et al., 2020c). Recently, the potential was used to calculate the Peierls stress in Nb (Jian et al., 2021b) and describe the dislocation motion in nanolaminated Nb (Jian et al., 2021a). In addition, it was also implemented in the CuNb embedded-atom-method alloy potential (Zhang et al., 2013), which was then applied to simulate the plastic deformation in the Nb layer in the Cu/Nb nanolaminate (Martínez et al., 2014, 2016; Huang et al., 2017; Jian et al., 2021a).

To build the Nb nanolaminate, we start with two single crystal layers M and M' , as shown in Fig. 1(a). The axes x , y , and z in layer M are aligned respectively with the $[111]$, $[112]$, and $[1\bar{1}0]$ directions. The x' , y' , and z' axes in layer M' correspond to the $[\bar{1}\bar{1}1]$, $[\bar{1}\bar{1}2]$, and $[\bar{1}\bar{1}0]$ directions, respectively. Along the y (or y') direction, the M' layer has a constant layer thickness of $L' = 5$ nm and the thickness of layer M is varied from $L = 5, 10, 20, 30, 40, 50, 60$, to 70 nm to study the effect of layer thickness on CLS. The dimensions along the x (or x') and z (or z') directions are constant, i.e., 43×26 nm 2 . PBCs are applied along the x (or x')

and the y (or y') axes, while traction-free boundary conditions are imposed along the z (or z') axis. These boundary conditions are the same as those in our prior work on CLS (Jian et al., 2021a) and dislocation motion in single crystals (Jian et al., 2020, 2021b; Xu et al., 2021; Wang et al., 2021; Romero et al., 2022).

According to the lattice coordinates in M and M', the interfaces in Nb/Nb nanolaminates are CTBs. A total of 600 atomistic structures were obtained by shifting the crystalline layer M relative to M' along the two in-plane directions to create 100 rigid body translations and deleting one atom from the atom pair in the interface with respect to six different cutoff distances. After minimizing via the conjugate gradient algorithm the energy of all 600 structures, we select the structure with the lowest interface energy. In each case, the minimization process is terminated when one of the following criteria was satisfied (Xu et al., 2019a, 2020b): (1) the energy change between successive iterations divided by the most recent energy magnitude is less than or equal to 10^{-12} and (2) the length of the global force vector for all atoms is less than or equal to 10^{-12} eV/Å.

In all analytical theories, it is assumed that the confined dislocation within a layer spans the entire layer thickness and thus its initial line length in our MD models equals the layer thickness, which is consistent with the assumption in the theories. After building the Nb nanolaminate with the lowest interface energy, we introduce a perfect edge dislocation with Burgers vector \mathbf{b} to layer M or both layers by deleting three $(1\bar{1}\bar{1})$ or $(\bar{1}\bar{1}1)$ atomic planes in the corresponding layers. Here, $\mathbf{b} = (a_0/2)\langle 111 \rangle$ and a_0 is the lattice parameter of 3.3008 Å. Note that the length (x dimension) and height (z dimension) of M layer are constant and only its layer thickness (y dimension) is varied. In this way, the variation in the layer thickness does not change the dislocation density in this layer. For classification, if the edge dislocation is only inserted into the M layer, the cases are referred to as “Alt-NL”, conveying that due to PBCs, the dislocations lie alternatively in neighboring layers of nanolaminate (see Fig. 1(a)). If an edge dislocation is placed into both the M and M' layers, the cases are named “All-NL”, since dislocations exist in all layers of the nanolaminate. For this case, their Burgers vectors can have either the same direction or opposing directions, denoted by “All-NL-S” (Fig. 1(b)) or “All-NL-O” (Fig. 1(c)), respectively. Furthermore, the spacing d between the glide planes of these two dislocations is varied from 0, 2.5 nm, to 5 nm. Note that the original interfaces in nanolaminated Nb contain no interfacial dislocations, while the inserted edge dislocation can create misfit dislocations at the interfaces, as shown in Fig. 1(a–c). For comparison, nanofilm MD models are built by bounding layer M between two traction-free surfaces along the y direction.

The NPT ensembles are then utilized to keep a low temperature (1 K) to minimize the influence of thermal fluctuations. This temperature is also used during subsequent loading. As shown in Fig. 1(a), the boundary condition of nanolaminated Nb along z direction is non-periodic initially, while those along x and y directions are periodic. During thermal relaxation, the NPT ensemble requires PBCs along all three directions. In this way, we need to maintain free surfaces of the MD model along z direction when the boundary condition along this direction is changed from non-periodic to periodic during thermal relaxation. Thus, two vacuum regions, above and below the free surfaces along the z -axis are created respectively in the Nb/Nb nanolaminate configurations when we conduct thermal relaxation in the system under the NPT ensemble. After thermal relaxation, the vacuum regions are removed and the boundary conditions along the z -axis return to being non-periodic. By contrast, the initial boundary conditions of Nb nanofilm along y and z directions are non-periodic, while only that along x direction is periodic. In this case, the free surfaces of its atomic configuration along y and z directions are maintained when the boundary conditions along these two directions are changed from non-periodic to periodic during thermal relaxation. When thermal relaxation in the nanofilm system is conducted under the NPT ensemble, four vacuum regions above and below the free surfaces along y - and z -axes are added, respectively. Similarly, these vacuum regions are removed after relaxation and the non-periodic boundary conditions along both y - and z -axes are recovered.

Next, as displayed in Fig. 1(d), the relaxed configurations are divided into the boundary region, the thermostat region, and the non-thermostat region, ranging from the free surfaces to the glide plane of the dislocation along the z -axis. Each of these regions possesses a thickness of 1 nm, 4 nm, and 16 nm, respectively. The NVE ensemble is imposed on the boundary and non-thermostat regions, while the NVT ensemble is applied to the thermostat regions to keep a constant temperature of 1 K. The utilization of the non-thermostat region, where the inserted dislocations glides, aims to reduce the artificial friction of thermostat (Cho et al., 2017; Dang et al., 2019; Jian et al., 2020, 2021a). Using the flexible boundary condition developed by Rodney (2007), we tailored separately and dynamically the velocities of the top and bottom boundary regions to keep the bottom boundary static and the top boundary moving at a constant velocity v that corresponds to a constant strain rate of 10^7 s $^{-1}$. The detailed operation is that we calculate the averaged velocities v_t and v_b of the top and bottom boundary regions at each step and then add the additional velocities $v - v_t$ and $-v_b$ to each atom in the top and bottom boundary regions, respectively. During shear loading, the total forces of boundary regions are maintained at zero. More details on thermal relaxation and shear loading can be found in (Jian et al., 2020, 2021a). To visualize the atomic configurations and analyze dislocation glide behavior, we employ the adaptive common neighbor analysis (Stukowski et al., 2012) implemented in OVITO (Stukowski, 2009).

As mentioned in the Introduction, the core cutoff parameter is $\alpha = b/r_{\text{core}}$. To calculate α , we obtain the value of r_{core} . To begin, we build a single crystal Nb atomic configuration with its crystallographic orientations the same as those of the M layer and its dimensions as 50.2 (x) \times 4.9 (y) \times 50.2 (z) nm 3 . The boundary conditions of the atomic configuration are the same as those of the CLS configurations. Specifically, the PBCs are applied in the x and y directions, while the traction-free boundary condition is applied in the z direction. After inserting the edge dislocation with $\mathbf{b} = (a_0/2)\langle 111 \rangle$ to the center of the atomic model, the energy of the entire system is minimized. With this, the total strain energy E of all atoms in the cylinder in Fig. 2(a) as a function of its radius r is obtained in Fig. 2(b). Here, E is the total potential energy minus the atomic cohesive energy for per unit length of dislocation line. Since elasticity theory predicts a logarithmic relation between E and r (Hirth and Lothe, 1982), r_{core} can be determined from the point in the $E - r$ curve, where E starts to vary with r logarithmically. More details on the calculation can be found in (Ossetsky and Bacon, 2003; Xu et al., 2016a; Lehtinen et al., 2016).

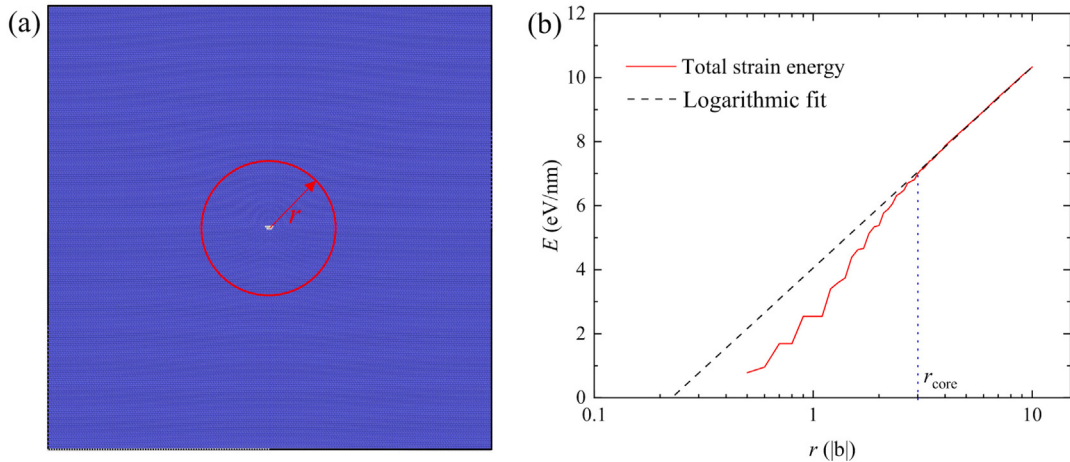


Fig. 2. (a) The schematic for Nb atomic configuration where the atoms in a cylinder with the radius of r are chosen to calculate the total strain energy. BCC atoms and those with unknown coordination structure are colored in blue and gray, respectively. (b) Total strain energy E of all atoms in the cylinder in (a) as a function of its radius r for an edge dislocation with $\mathbf{b} = (a_0/2)\langle 111 \rangle$ on the $\{110\}$ glide plane in Nb. The radius of dislocation core r_{core} can be determined from the point in the $E - r$ curve, where E starts to vary with r logarithmically. (For interpretation of the references to color in this figure legend, the reader is referred to the web version of this article.)

3. Theoretical models

In this section, we revisit previously proposed analytical models for the critical stresses for CLS and introduce a modified model, since they all will be tested later against the MD calculations. One of the CLS models is composed of three terms (Misra et al., 2005), where the first term addresses line tension as the dislocation bows out between the interfaces, which is described by the Orowan-like relation (Orowan, 1934). The second and third terms are related to interface effect and the resistance from interfacial dislocation array, respectively. Since there are no interfacial dislocations in the original coherent interfaces of the Nb nanolaminate and nanofilm considered here, the third term is not included in the present analysis. Also because we will calculate the critical value of the resolved shear stress applied in the glide plane and direction of the dislocation, we remove the Taylor factor T that converts from local shear to normal stress. With these two considerations we rewrite Eq. (6) to obtain the first model for the CLS glide resistance τ_L as

$$\tau_L = m \frac{Gb}{L} \ln \left(\frac{\alpha L}{b} \right) - \frac{f}{L}, \quad (9)$$

where m is a material parameter and as mentioned, f is the change in interface energy with straining. It depends on the properties of the interface and it was normalized by L to give the term f/L with dimension of stress.

If we more strictly apply Eq. (6) to the particular stress/single crystalline layer orientation considered here, then the parameter χ is 90° , and m in Eq. (9) is equal to $(4 - v)/[8\pi(1 - v)]$. These substitutions give a slightly different expression for the CLS shear stress, denoted by τ_M :

$$\tau_M = \frac{Gb}{8\pi L} \left(\frac{4 - v}{1 - v} \right) \left[\ln \frac{\alpha L}{b} \right] - \frac{f}{L}. \quad (10)$$

Next, we consider a new model that involves two terms, where the first term is due to line tension, as before, and the second term arises from the interface-dislocation interaction. Again, since the interfaces are coherent, the additional resistance from interfacial dislocations is not included. With these considerations, the CLS model, denoted by τ_f , becomes

$$\tau_f = m \frac{Gb}{L} \ln \left(\frac{\alpha L}{b} \right) + f_{\text{int}}, \quad (11)$$

where f_{int} represents an interface resistance resulting from interface-dislocation interaction. It is dependent on the properties of the interface but independent of L . The coefficient m is retained as a material parameter. According to Fig. 2, r_{core} is $3b$ and thus, $\alpha = b/r_{\text{core}} = 0.333$ for the models shown above.

As a final model, we consider an equivalent shear stress for CLS for the Hall-Petch model in Eq. (7), given by

$$\tau_{\text{HP}} = \tau_0 + \frac{k}{\sqrt{L}}. \quad (12)$$

where τ_0 is the slip resistance in the crystalline layer, without the influence of the interface, and k is the Hall-Petch-like coefficient.

In what follows, we will compare results from MD simulations of CLS in Nb with these four models, τ_L , τ_M , τ_f , and τ_{HP} . For Nb, b , v , and G are 0.286 nm, 0.398, and 37.5 GPa, respectively. The latter two are effective isotropic values for Nb obtained using the Hill average (Xu et al., 2019b). Thus, $(4 - v)/[8\pi(1 - v)] = 0.238$ in the τ_M model.

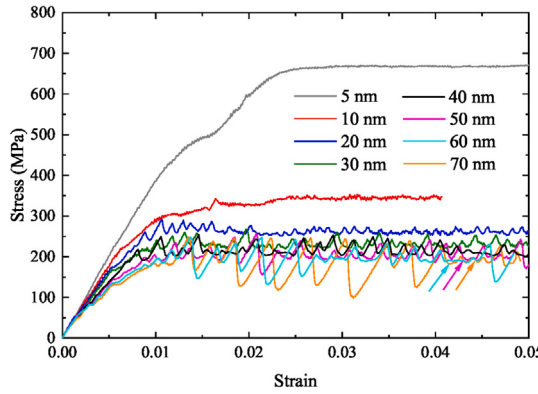


Fig. 3. Shear stress–strain curves in the Alt-NL configurations. Here, Alt-NL denotes the nanolaminate with a gliding dislocation confined in the layer M while the neighboring layer M' is dislocation-free. The layer thickness of M' is constant with $L' = 5$ nm, while that of M varies: $L = 5, 10, 20, 30, 40, 50, 60$, and 70 nm. Due to PBCs along the y direction, dislocations exist alternatively in the neighboring layers. When $L \geq 50$ nm, the stress fluctuates significantly around a nominal value, as shown by the corresponding arrow, which is referred as the plateau stress.

4. Results

4.1. Effect of layer thickness

4.1.1. CLS in Alt-NL configurations

In some deformed nanolaminates, only a few layers have a moving dislocation, because these layers may have a weaker dislocation source or be much more favorably oriented for glide than the adjacent layers. In these cases, CLS occurs in one layer but not the neighboring layers. We study this configuration, called Alt-NL, which is also the commonly studied configuration, in this section.

Fig. 3 compares the shear stress–strain curves in the Alt-NL configurations with various layer thickness L for the M layer. In Fig. 3, the shear stress rises and eventually plateaus. As L increases from 5 nm to 40 nm, the plateau stress decreases from 668.0 MPa to 211.8 MPa.

To correlate the stress–strain response with the motion of the dislocation, snapshots of dislocation glide for $L = 5$ nm are analyzed in Fig. 4(a–d). They reveal that the dislocation line remains nearly straight with little bow-out when it glides. In addition, the confined dislocation glides smoothly at a nearly constant rate, corresponding to the steady plateau stress for $L = 5$ nm. Furthermore, the final stress plateau for the CLS models with $5 \leq L \leq 40$ nm is similar, i.e., there is no significant stress oscillation on the plateau, suggesting a nearly uniform motion of CLS for $L = 5, 10, 20, 30$ and 40 nm. Since the shear stress is proportional to the glide speed of dislocation, the velocity of CLS decreases in the order of $L = 5, 10, 20, 30$ and 40 nm.

In contrast, the stress–strain responses for $L > 40$ nm exhibit significant oscillations around the plateau stresses. In this regime, for three cases, $L = 50, 60$ and 70 nm, the stress fluctuates significantly around a nominal value, as shown by the corresponding arrow, which we refer to hereinafter as the plateau stress. Further, the plateau stress has a weak dependence on L , decreasing only slightly as L increases from 40 nm to 60 nm and then remaining almost unchanged for 70 nm.

Analyzing the dislocation motion, we find that such severe stress oscillations are the result of staggered dislocation motion, described as the pinning and depinning of the two ends of the long dislocation line. As an example, Fig. 4(e–h) shows the dislocation motion in the case of $L = 70$ nm under shear loading. The dislocation line is almost straight in the beginning and then bows out ($\epsilon = 0.00375$), since one end moves faster than the other. As the leading bottom end moves, it drags the other end and bows out more significantly ($\epsilon = 0.01200$). As strain increases, glide of the bottom end experiences more resistance, while the top end accelerates to catch up with the bottom end ($\epsilon = 0.01875$). The dislocation glides by pinning and depinning from the interface, with the two ends of the dislocation alternating in taking the lead. As a result, this staggered glide occurs repeatedly. Thus, we find that as the initial dislocation length increases from 5 to 70 nm, the glide transitions from being smooth to staggered.

4.1.2. CLS in All-NL-S Configurations

After some amount of straining, it is likely that all layers in the laminate material, particularly if the layer material is the same, will have actively moving dislocations. In this section, we study the effect of dislocation glide in the neighboring M' layers on CLS, considering all dislocations share the same glide plane and glide at the same time along the same direction. We refer to this case as All-NL-S with $d = 0$ nm.

Fig. 5 shows the shear stress–strain curves of the All-NL-S configurations with $d = 0$ nm. Like the curves for the Alt-NL configurations, the stress in the All-NL-S configuration increases and then eventually reaches a plateau stress with an increasing strain. In contrast, none of the All-NL-S curves exhibit significant oscillations. Further, the plateau stress is substantially lower. For the same L , the plateau stress for the Alt-NL configuration is three to six times larger than that of the All-NL-S configuration. In

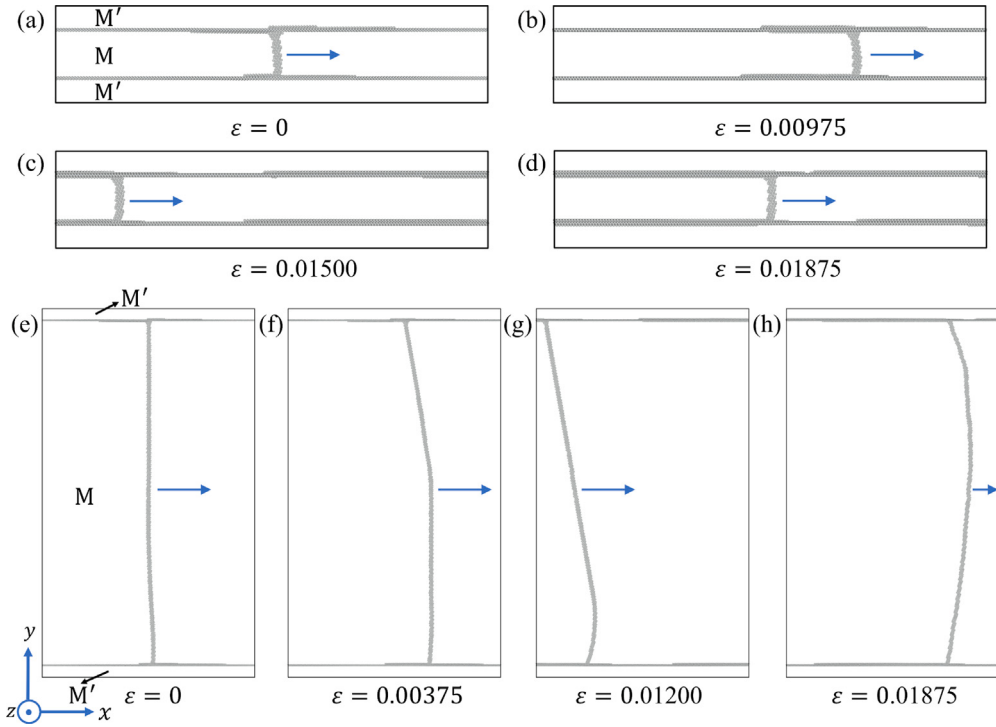


Fig. 4. Snapshots for dislocation glide in the Alt-NL configuration with the layer thickness (a-d) $L = 5 \text{ nm}$ and (e-h) $L = 70 \text{ nm}$. The blue arrows denote the CLS directions.

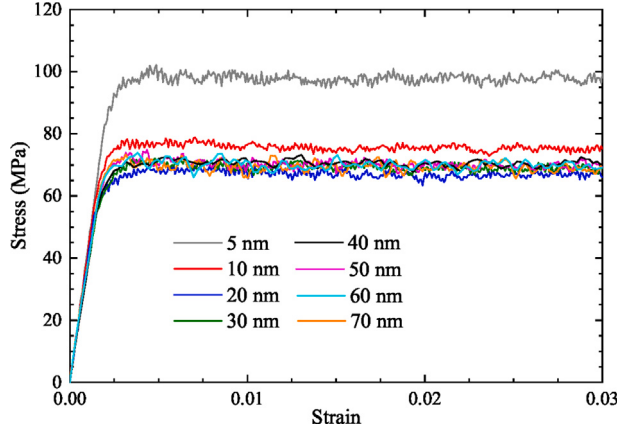


Fig. 5. Shear stress–strain curves in the All-NL-S configurations. Here, All-NL-S denotes the nanolaminates has a gliding dislocation in both M and M' layers and these two dislocations share the same Burgers vectors **b**. The gliding planes are aligned, i.e., their separation $d = 0 \text{ nm}$. The layer thickness of M' is constant with $L' = 5 \text{ nm}$, while that of M varies with $L = 5, 10, 20, 30, 40, 50, 60$, and 70 nm .

other words, CLS in all the layers is much easier than that in alternate or separated layers. Another key difference is the weak layer thickness effect on strength. As L increases from 5 nm to 70 nm, the plateau stresses only decrease from 97.7 MPa to 69.2 MPa, which is 1/16 of the stress reduction in the Alt-NL configuration.

The different responses suggest different modes of dislocation motion. Fig. 6 compares the dislocation morphology at different times for the finest $L = 5 \text{ nm}$ and coarsest $L = 70 \text{ nm}$ layer thicknesses in the All-NL-S configurations. When $L = 5 \text{ nm}$, in Fig. 6(a-d), the dislocations in both M and M' move at the same velocity. Their line morphology is almost straight and steady. This smooth gliding behavior is like that of the Alt-NL configuration for the same layer thickness $L = 5 \text{ nm}$. Similarly, when $L = 70 \text{ nm}$, in Fig. 6(e-h), the dislocation line in the M layer also remains nearly straight and moves at the same rate as the dislocation in the neighboring M' layer. In all All-NL-S cases, regardless of L , glide is smooth, and not staggered, throughout the entire straining period, explaining the lack of stress oscillations in the stress–strain curve. Also, the dislocation does not bow out significantly, indicating that the

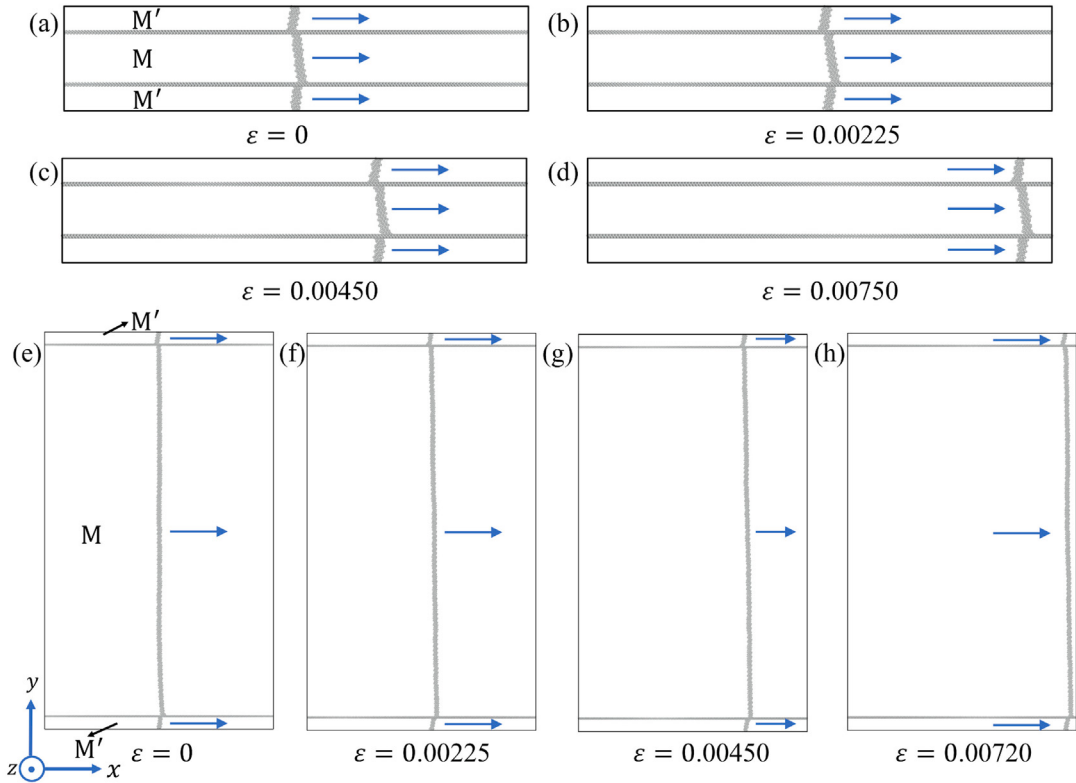


Fig. 6. Simulation snapshots of the edge dislocations gliding in the M and M' layers. The layer thickness of M' is $L' = 5$ nm and that of M is (a–d) $L = 5$ nm and (e–h) $L = 70$ nm. The blue arrows denote the CLS directions. The definition of All-NL-S is the same as that in Fig. 5 and the gliding planes of these two dislocations are aligned, i.e., separation $d = 0$ nm.

interfaces are not imposing enhanced resistance relative to the interior of the crystal. When dislocations in neighboring layers glide in concert, they relieve the resistance imparted by the interface. The constraint provided by the layer thickness L is reduced, leading to a weakened layer size effect.

To understand the effect of the neighboring gliding dislocations, we first study the interface/dislocation junctions with and without neighboring dislocation, corresponding to the All-NL-S cases and Alt-NL cases, respectively. Fig. 7 compares the y -axis height maps and stress fields of the interface in the vicinity of the junction for the Alt-NL and All-NL-S configurations. The height maps in Fig. 7 indicate the amount the interface protrudes out at the dislocation/interface junction. In Alt-NL cases, an interface ledge, approximately 3 Å in height, forms at the dislocation/interface junction at each end of the dislocation. In All-NL-S cases, however, the interface is planar without a ledge.

As shown in Fig. 1(a), the inserted edge dislocation BC in Alt-NL configuration creates the misfit edge dislocations AB and CD at the interfaces, which results in the interface ledge at each interface. When the confined dislocation BC moves, denoted by B'C', it drags two misfit screw dislocations (BB' and CC'). By contrast, the misfit edge dislocations (AB and CD) at the interfaces remain stationary during loading. As shown in Fig. 1(b), the inserted edge dislocations BC and DA in All-NL-S configuration create the misfit edge dislocations AB and CD at the interfaces. When the confined dislocations BC and DA move, denoted respectively by B'C' and D'A', they drag four misfit screw dislocations, i.e., AA', B'B, C'C and DD', among which AA' and B'B (or C'C and DD') have the opposite line directions. By contrast, the misfit edge dislocations (AB and CD) remain stationary during loading. In this section, we consider $d = 0$ nm, and thus the inserted edge dislocations BC and DA do not generate the misfit edge and screw dislocations at the interfaces in the beginning and during shear loading. Namely, $d = 0$ nm results in the disappearance of AB, CD, AA', B'B, C'C and DD'. Therefore, there is no ledge at the interface for All-NL-S cases with $d = 0$ nm.

The calculated τ_{xz} shear stress fields at each interface are compared in Fig. 7. This component helps to drive the dislocation as it moves from left to right in the direction of the Burgers vector. In Alt-NL cases, with the ledge, the fields are positive in the direction of motion; however, they differ between the two interfaces. This explains the staggered motion of the dislocation. Under an applied shear, it can depin more easily from one end compared to the other. The initial ledges and fields do not change with layer thickness. However, the distance moved after each end depins is proportional to the dislocation length. When each end of the $L = 70$ nm dislocation depins, it moves forward in large increments, leading to pronounced oscillations. In contrast, in All-NL-S cases, fields are stronger, exhibiting a mirror symmetry about the z direction, and equal at the two interface/dislocation junctions. The interface shear τ_{xz} provides supporting and equal driving forces on both sides of the dislocation. Glide is smooth and dislocation bow-out is extremely slight for all layer thicknesses.

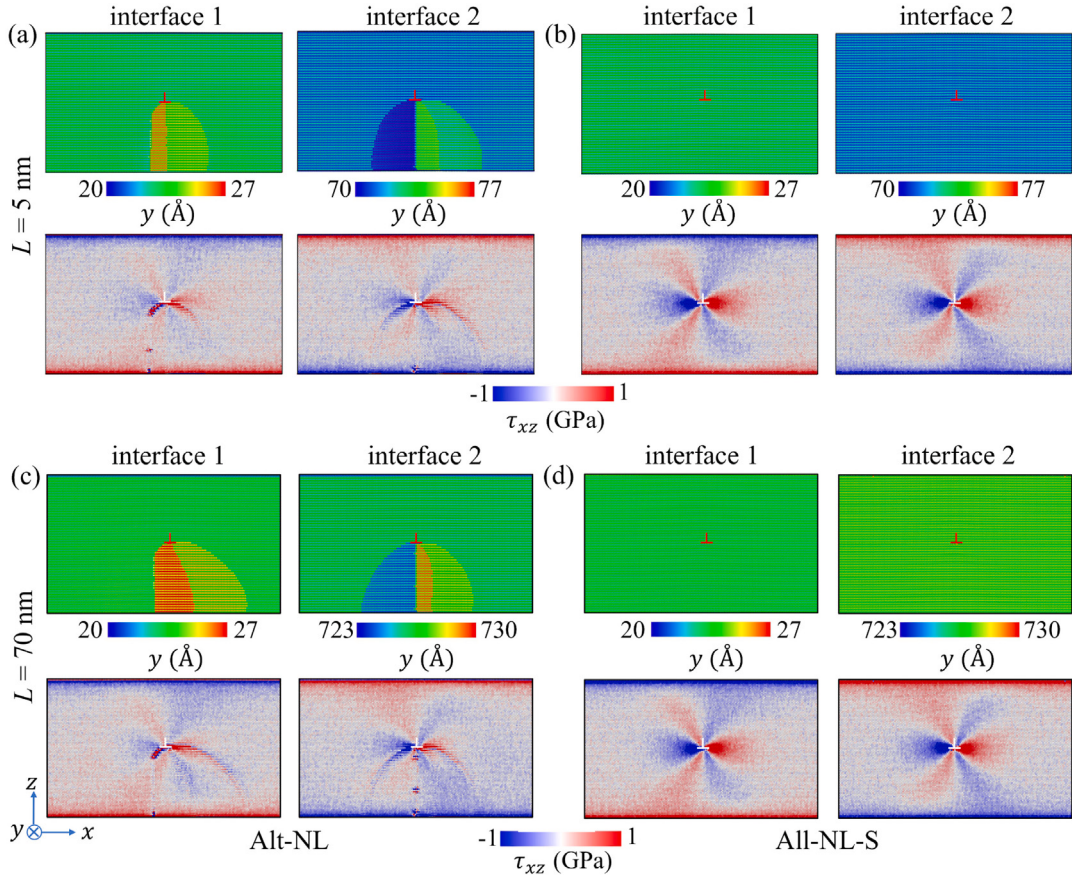


Fig. 7. The initial atomic structures of interfaces 1 and 2 for (a)–(b) $L = 5\text{ nm}$ in the (a) Alt-NL and (b) All-NL-S configurations, and (c)–(d) $L = 70\text{ nm}$ in the (c) Alt-NL and (d) All-NL-S configurations. The atoms are colored according to their atomic coordinates along the y axis and the shear stress component τ_{xz} . For All-NL-S, the glide planes of the dislocations in M and M' layers are aligned, i.e., $d = 0\text{ nm}$. Interfaces 1 and 2 are demonstrated in Fig. 1(a), while '1' denotes the edge dislocation. (For interpretation of the references to color in this figure legend, the reader is referred to the web version of this article.)

4.1.3. CLS in nanofilm configurations

In order to understand the effect of the coherent interface, we consider the case with the same layer M but with free surfaces and compare it to the Alt-NL case with no dislocations gliding in the neighboring layers. This comparison intends to reveal whether the free surface plays the similar role to the coherent interface in the CLS behavior and imposes a similar layer size effect on strength. Fig. 8 shows the shear stress–strain curves for the CLS behaviors in the nanofilm configurations. In all curves, the stress rises to a first peak and then drops, followed by one or more fluctuations with more strain. Finally, a plateau stress is reached. As L increases from 5 nm to 40 nm, the plateau stress drops from 139.5 MPa to 98.2 MPa. For larger L , the plateau stresses remain almost unchanged and unaffected by L . For the same L , these stresses are much lower than those for the Alt-NL configurations. The free surface provides much less resistance to dislocation glide than the CTBs. This result is not directly related to interface energy. The CTB in the Alt-NL has a lower boundary energy of 137.4 mJ/m² than the {112} free surface in Nb, 1962 mJ/m² (Jian et al., 2021a). An analysis of the free surface/dislocation junction sites indicate that the free surface is planar with no ledges. A comparison with the Alt-NL case suggests that the creation of the ledge and consequential strain energy penalty in the interface in the Alt-NL case enhanced the resistance to CLS.

In Fig. 9, we present the motion of the dislocation in the nanofilm for two extreme layer thicknesses $L = 5\text{ nm}$ and $L = 70\text{ nm}$. In both cases, the dislocation bows out and moves in a staggered fashion, pinning and depinning at its ends. The stress–strain response, as a result, oscillates. Compared with the Alt-NL, the staggered glide is stronger in the nanofilm. After some amount of strain, the dislocation adjusts itself to reduce its curvature and glides in a smooth manner. This transition to smooth glide results in the steady plateau stress seen in the stress–strain response. In steady-state, the gliding dislocation is almost straight for $L = 5\text{ nm}$ but slightly bowed out for $L = 70\text{ nm}$. The reduced bow-out when in the nanofilm indicates that the free surface posed little resistance to CLS.

4.1.4. Layer size effect on strength

Fig. 10 compares the variation in critical shear stress with L for the CLS in the nanolaminate and nanofilm. For this analysis, we use the plateau stresses in the stress–strain curves in Fig. 3, Fig. 5, and Fig. 8 as the critical stresses. In all cases, the size effect

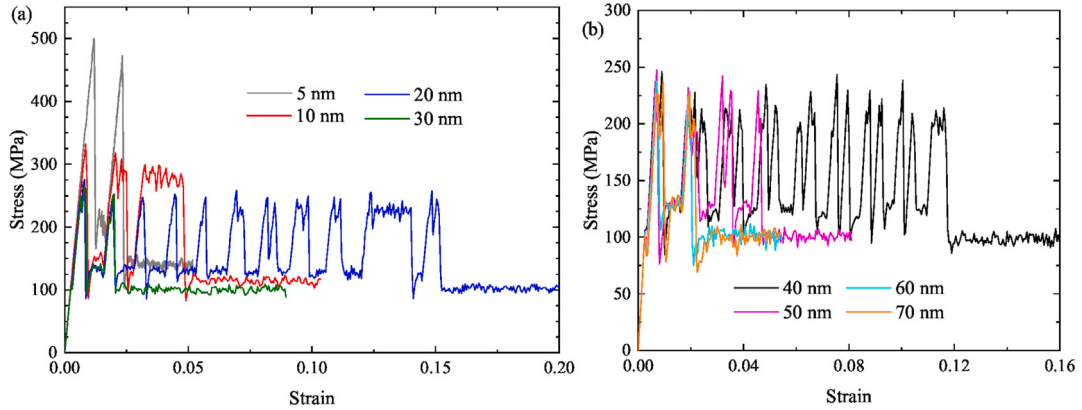


Fig. 8. Shear stress–strain curves in the nanofilm configurations. (a) compares the response for layer thicknesses $L = 5, 10, 20$, and 30 nm , and (b) $L = 40, 50, 60$, and 70 nm . In the nanofilm, the dislocation glide is confined between two free surfaces.

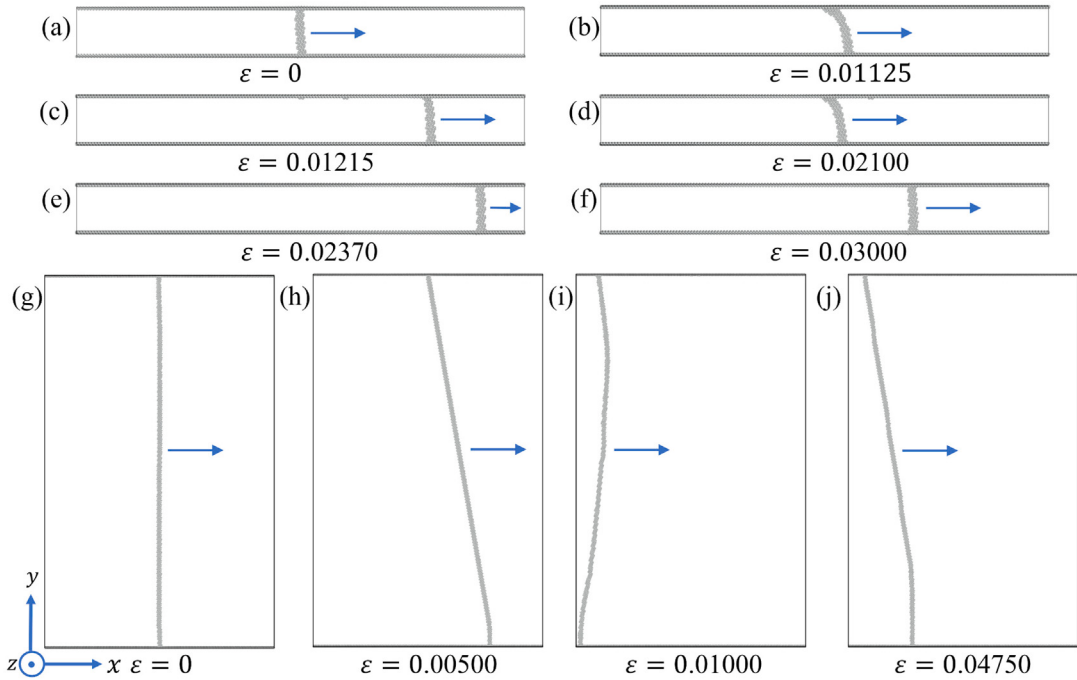


Fig. 9. Simulation snapshots for dislocation glide in the nanofilm configuration with the layer thickness of (a–f) $L = 5\text{ nm}$ and (g–j) $L = 70\text{ nm}$. The blue arrows denote the glide directions of dislocations.

is negative, that is, the stress decays as L increases and there is no sign of an inverse size effect for the range of L studied. As L increases beyond 30 nm , the size effect diminishes. For the classic case, Alt-NL, in which an isolated dislocation threads between two interfaces, the resistance is the highest and the layer size effect the strongest. For comparison, the plateau shear stress to move an edge dislocation on the $\{110\}$ plane of a Nb single crystal is indicated on the plot. This plateau stress, approximately 66 MPa (Jian et al., 2021a) at 1 K , is found to be nearly independent of L . As shown, the shear stress for the All-NL-S case is close to that for an isolated dislocation. When dislocations glide in all layers on the same plane, the constraining effect of the interfaces is nearly removed.

4.1.5. Comparison with analytical models

Fig. 11 compares the predictions of four strength models with the MD results for the Alt-NL and All-NL-S and nanofilm cases. The corresponding parameters are listed in Table A.1–Table A.4, respectively. As shown, τ_f and τ_{HP} provide the best fits to the MD data in all cases, with the τ_f performing better. In contrast, for the All-NL-S and nanofilm cases, the τ_L and τ_M models have an inflection point at $L \approx 10\text{ nm}$, below which the stress decreases with decreasing L .

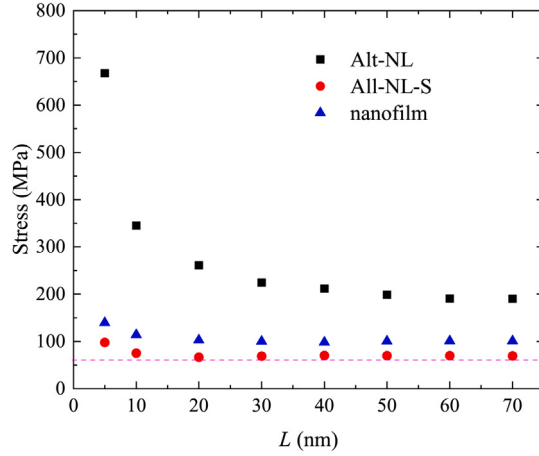


Fig. 10. The plateau flow stress as the function of layer thickness L in the Alt-NL, All-NL-S and nanofilm configurations. Here, the definitions of Alt-NL and All-NL-S are the same as those in Figs. 3 and 5, respectively. The plateau flow stresses are summarized from the stress-strain curves in Fig. 3, Fig. 5, and Fig. 8. For reference, the plateau shear stress to move the same edge dislocation in Nb single crystal without interfaces or free surfaces is also indicated by the dashed line. The value of this plateau stress is 66 MPa (Jian et al., 2021a).

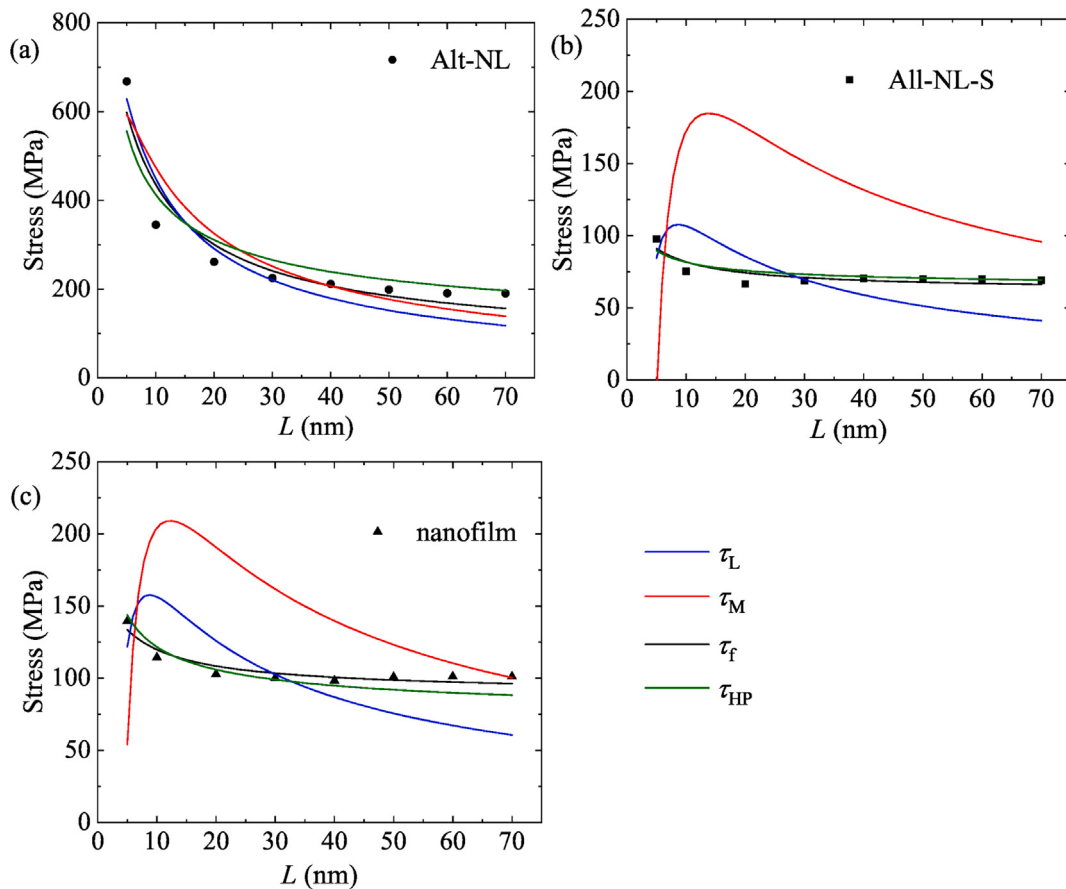


Fig. 11. Comparison among the analytical curves for Eq. (9)–Eq. (12) with the (a) Alt-NL, (b) All-NL-S, and (c) nanofilm configurations. The definitions of Alt-NL and All-NL-S are consistent with those in Fig. 3 and Fig. 5, respectively. The parameters for each analytical model are given in Table A.1–Table A.4 in the appendix.

To obtain agreement, we find that interface resistance parameter f_{int} of the τ_f model is approximately 61 MPa for the Alt-NL and All-NL-S and slightly higher for the nanofilm at about 88 MPa (see Table A.3). This can be expected since the CTB interface is the same in the two former configurations and its energy (137.4 mJ/m^2) is smaller than the free surface energy (1962 mJ/m^2) for the $\{112\}$ surface in Nb (Jian et al., 2021a). Note that we compare the interface energy of CTB with and without a screw dislocation in Fig. C.2 in the Appendix. The result shows that the appearance of misfit screw dislocation at the interface does not change significantly the interface energy that is only enhanced by 28.9 mJ/m^2 . The free surface energy for the $\{112\}$ surface in Nb is much larger than the interface energy of the original CTB without screw dislocation. However, the large difference of 1824.6 mJ/m^2 only causes an increase of 27 MPa in f_{int} . Thus, it is reasonable that f_{int} is almost the same for Alt-NL and All-NL-S (61 MPa), which have the interfaces with and without screw dislocations when shear loading starts, respectively (see Fig. 1(a) and (b)). Thus, we think the effect of misfit screw dislocation on the CLS is not significant and does not influence the accuracy of our proposed τ_f model.

In τ_f model (Eq. (11)), the parameter m in its Orowan bowing term is positively associated with the bowing-out degree of dislocation line. According to the fitting results of m in Table A.3 in the Appendix, the parameter m in the τ_f model increases in the order of All-NL-S (0.00801), nanofilm (0.0120), and Alt-NL (0.142), implying that the dislocation line in the corresponding configuration bows out more significantly in Alt-NL than in the nanofilm and All-NL-S. This is in agreement with the MD observations in Fig. 4, Fig. 6, and Fig. 9. $m = 0.00801$ for All-NL-S is tiny, suggesting that the dislocation line bows out extremely slightly and looks almost straight. Since f_{int} , i.e., interface resistance, is close in Alt-NL and All-NL-S, it is m or the dislocation line tension that explains their differences in flow stress. Due to the enhanced resistance at the interface created by the ledges compared to that in the interior, the dislocation bows out and overcomes line tension.

For the τ_{HP} model parameters, τ_0 is intended to represent the lattice resistance to dislocation motion, while k represents the barrier effect from the interface. For various configurations, $\tau_0 \approx 66 \text{ MPa}$ for Alt-NL, 62 MPa for All-NL-S, and 68 MPa for the nanofilm. They are all close to the flow stress to move the edge dislocation in a Nb single crystal (66 MPa), consistent with the theory. The finding that the τ_{HP} describes well MD strength- L data is reasonable. Hall-Petch relation is an empirical model and the explanations, such as the pile ups of dislocations, came later. Thus, Hall-Petch relation can also apply to the situations without pile ups. Similarly, Subedi et al. (2018) demonstrated that the Hall-Petch model captured well the size effect on the strength of many nanotwinned and bimetal nanolaminate systems when $L > 5 \text{ nm}$, even though pile ups are not expected in such fine nanolayers. They showed that a dislocation density accumulation in the interfaces could give rise to the $1/\sqrt{L}$ scaling. Also, using a stochastic grain boundary dislocation emission model rather than a pile up model, Chen et al. (2020) were able to predict the experimentally observed Hall-Petch scaling in the strength of Cu/Nb nanolaminates.

4.2. Effect of dislocation distribution

Up to now, we have considered the situation in which the confined dislocations in all layers share the same glide plane ($d = 0 \text{ nm}$) and Burgers vector. However, it is statistically more likely that their glide planes would be separated, i.e., $d > 0 \text{ nm}$. The dislocation can glide on any of the parallel planes since they all have similar driving forces. Which plane dislocation will glide on is envisioned to depend on other factors, such as the location of the dislocation source in the boundary. In this section, we consider the case in which dislocations in neighboring layers glide in the slip planes that are not aligned but separated by a distance d , as shown in Fig. 1(b–c). In these calculations, both M and M' layers have the same thickness of $L = L' = 5 \text{ nm}$.

4.2.1. CLS behavior with the same glide direction in the adjacent layers

We simulate dislocation motion among like-signed dislocations but that are separated by distances $d = 2.5 \text{ nm}$ or 5 nm . Fig. 12 shows the stress-strain response for these two situations compared with the prior case of aligned planes ($d = 0 \text{ nm}$). In all cases, the stresses rise along the same path but reach three different peak plateaus. As the straining proceeds, the stresses remain stable without oscillations. The effect of d on the resistance to glide is strong, with greater separation leading to a higher resistance. It can be expected that if d increases further, the flow stress would only increase to that corresponding to no neighboring dislocation (668 MPa for the Alt-NL case).

Fig. 6(a–d) and Fig. 13 show the motion sequence for $d = 0 \text{ nm}$ and $d = 5 \text{ nm}$, respectively. The CLS behavior in these two configurations are similar; namely, in the same configuration, dislocations in both M and M' layers remain nearly straight and glide smoothly at the same velocity. The separated distance d does not change the dislocation line morphology for the CLS in All-NL-S configuration. Throughout their glide process in all configurations, the dislocations in M and M' layers remain in their original glide planes and their separated spacing d does not get closer or wider. Therefore, the relative positions between these two dislocations along the x direction is unchanged.

The interaction between these like-signed dislocations changes the resistance provided by the interface. To understand the effect of d , the initial atomic structures of interfaces 1 and 2 for $d = 2.5 \text{ nm}$ and $d = 5 \text{ nm}$ are analyzed in Fig. 14. Unlike when the dislocations glide on the same plane, $d = 0 \text{ nm}$ in Fig. 7(b), both interfaces contain 3 \AA tall ledges at the interface/dislocation junctions when $d > 0 \text{ nm}$. The extent of the ledges increases as d increases, which can be explained by Fig. 1(b). As shown in Fig. 1(b), the inserted edge dislocations BC and DA with $d > 0 \text{ nm}$ generate the misfit edge dislocations AB and CD at the interfaces, whose line lengths are equal to d and positively associated with the ledge area. The increasing ledge area heightens the energy barrier for the CLS, which translates to the higher plateau stress. From the corresponding τ_{xz} stress distributions in Fig. 14, like the $d = 0 \text{ nm}$ case, the τ_{xz} distributions are nearly equal at both interface/dislocation junctions, giving rise to equal resistance on both sides. This explains the synchronous CLS motion among the dislocations.

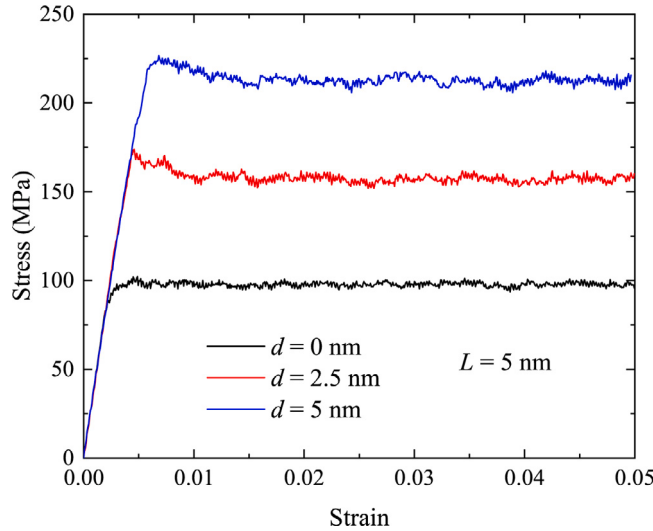


Fig. 12. Shear stress–strain curves in All-NL-S configurations with the same $L = 5 \text{ nm}$ and various d . Here, the definition of All-NL-S is consistent with that in Fig. 5 and d represents the distance the glide planes of the dislocations in the neighboring M and M' layers are separated.

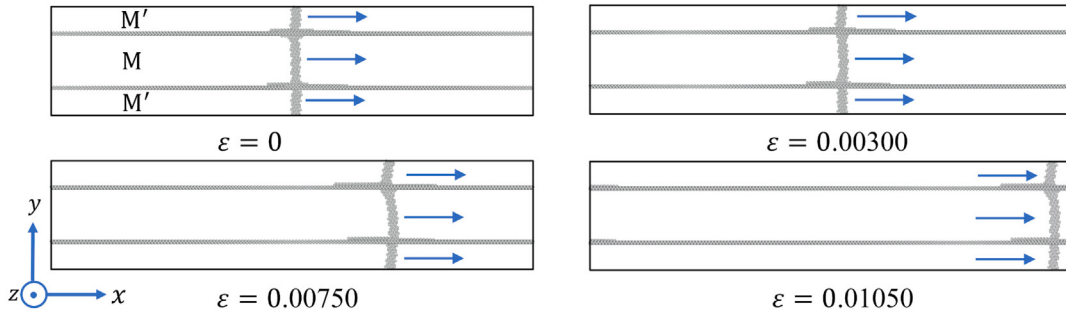


Fig. 13. Snapshots for the edge dislocations gliding in both the M and M' layers in the All-NL-S configurations with $d = 5 \text{ nm}$. The blue arrows denote the CLS directions.

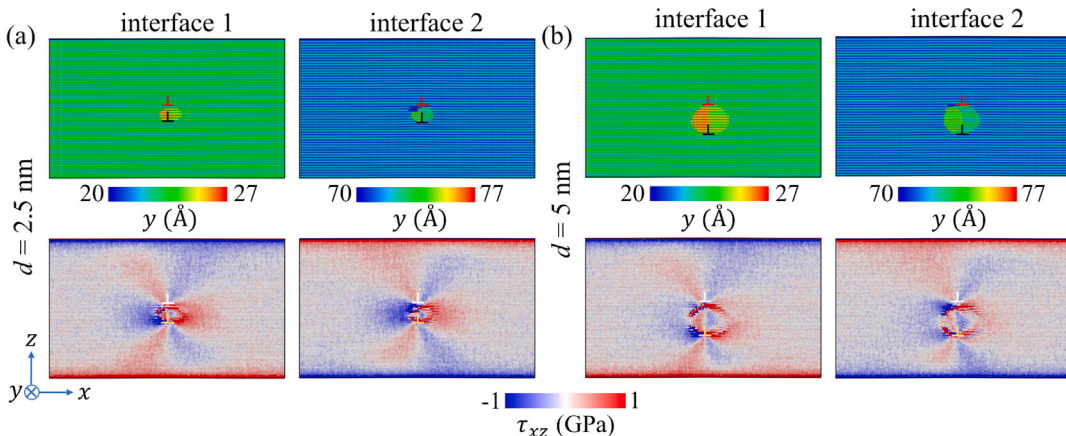


Fig. 14. The initial atomic structures of interfaces 1 and 2 in the All-NL-S configurations with (a) $d = 2.5 \text{ nm}$ and (b) $d = 5 \text{ nm}$. Definitions of All-NL-S and d are the same as those in Fig. 12. The atoms are colored according to their atomic coordinates along the y axis or the shear stress component τ_{xz} . Interfaces 1 and 2 are shown in Fig. 1(a), while ‘ \perp ’ denotes the edge dislocation. (For interpretation of the references to color in this figure legend, the reader is referred to the web version of this article.)

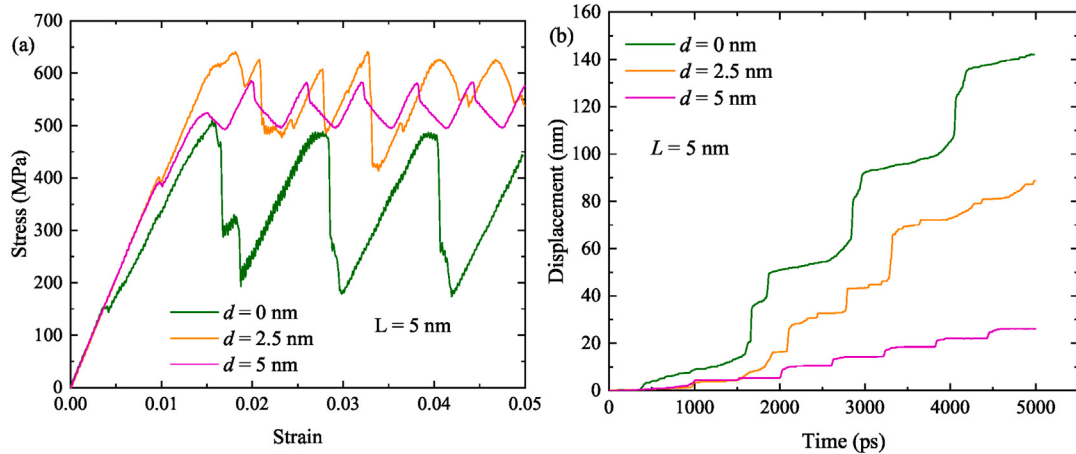


Fig. 15. (a) Shear stress–strain curves in All-NL-O configurations with $L = 5 \text{ nm}$ and (b) displacement–time curves for the confined dislocations in their M layers. The definition of d is the same as that in Fig. 12 and All-NL-O refers to dislocations in the M and M' layers with opposite Burgers vectors.

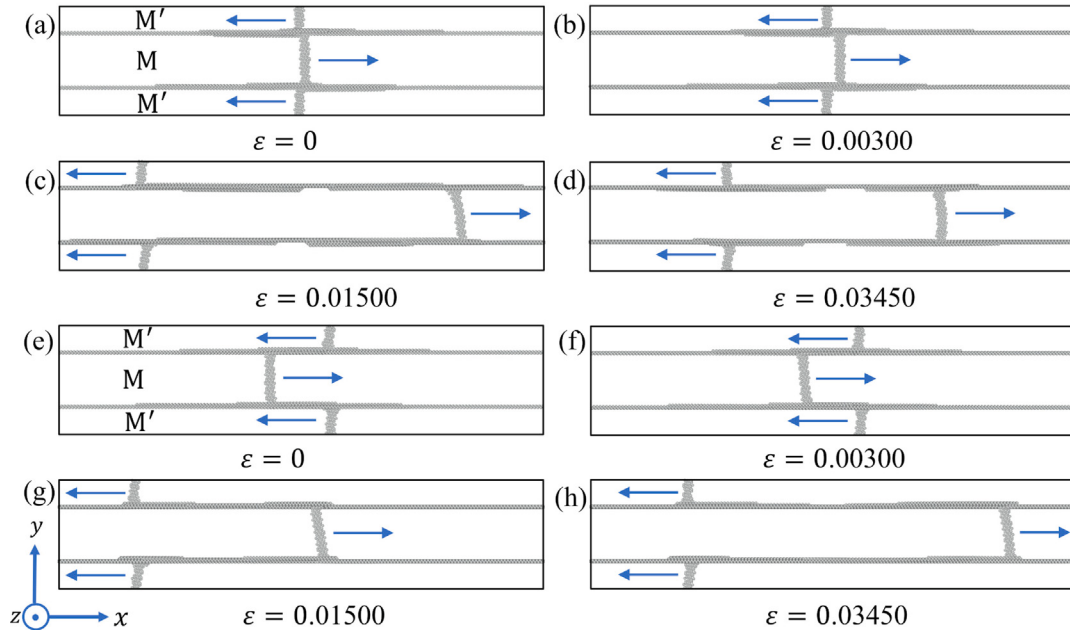


Fig. 16. Snapshots for the edge dislocations gliding in the M and M' layers of the All-NL-O configurations with (a–d) $d = 0 \text{ nm}$ and (e–h) $d = 5 \text{ nm}$. Definitions of All-NL-O and d are the same as those in Fig. 15. The blue arrows denote the CLS directions.

4.2.2. CLS behavior with the opposite glide directions in the adjacent layers

Next, we simulate dislocation motion among opposite-signed dislocations that are also separated by distances $d = 0 \text{ nm}$, 2.5 nm , or 5 nm . The stress–strain responses for these three situations are compared in Fig. 15(a).

In All-NL-O configurations, the dislocations in M and M' layers are oppositely signed and hence glide in the opposite directions under shear loading, as demonstrated in the snapshots for dislocation glide in the All-NL-O configurations with $d = 0 \text{ nm}$ and $d = 5 \text{ nm}$, in Fig. 16(a-d) and (e-h), respectively. For $d = 0 \text{ nm}$, the dislocations in M and M' layers do not shift away from each other during relaxation (Fig. 16(a)). By contrast, the nonzero d results in the shift of these two dislocations away from each other after relaxation and before loading (Fig. 16(e)). To gain more insight, we turn to the stress–strain curves of All-NL-O configurations.

Different from the shear stress–strain curves of All-NL-S configurations, the stress does not plateau but exhibits periodic stress oscillations in the curves of All-NL-O configurations, as displayed in Fig. 15(a). Among all these curves, $d = 0 \text{ nm}$ corresponds to

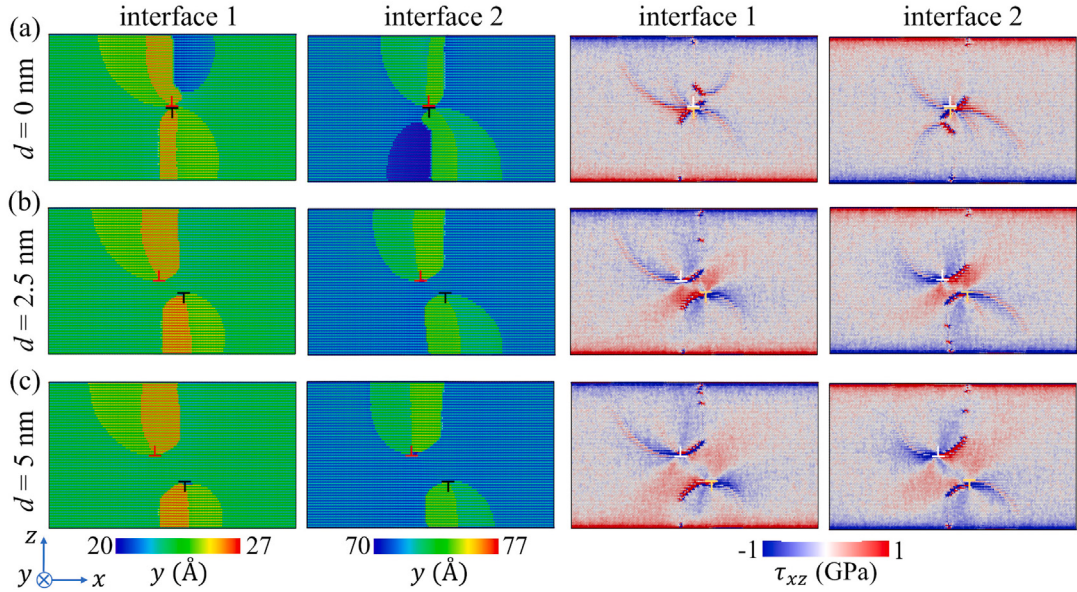


Fig. 17. The initial atomic structures of interfaces 1 and 2 in All-NL-O configurations with (a) $d = 0 \text{ nm}$, (b) $d = 2.5 \text{ nm}$, and (c) $d = 5 \text{ nm}$. The atoms are colored according to theirs atomic coordinates along the y axis and the shear stress component τ_{xz} . Definitions of All-NL-O and d are the same as those in Fig. 15. Interfaces 1 and 2 are shown Fig. 1(a), while 'L' and 'T' denote the edge dislocations with opposite Burgers vectors. (For interpretation of the references to color in this figure legend, the reader is referred to the web version of this article.)

the lowest peak stress (510.2 MPa), while $d = 2.5 \text{ nm}$ and $d = 5 \text{ nm}$ lead to higher peak stresses, i.e., 641.2 MPa and 585.4 MPa, respectively. Compared to the All-NL-S configurations (Fig. 12), the stresses in the All-NL-O configurations are higher, which can be a consequence of the larger ledges generated at the interfaces. The two bounding ledges are also unequal in shape. Unlike the cases in the All-NL-S configurations, the largest separated spacing d in the All-NL-O configurations does not lead to the highest peak stress. Instead, the amplitude of the stress fluctuations in these curves decreases from 317 MPa to 157 MPa and finally to 87 MPa, with d increasing from 0 to 2.5 nm and then 5 nm, respectively. Similar to All-NL-S configuration, it is also expected that when d increases to a large enough value, the stress fluctuation in All-NL-O configuration will diminish and the stress-strain response will behave in a similar way to that of the Alt-NL case. Corresponding to the stress fluctuations, the CLS motions in All-NL-O configurations are jerky.

We further present the displacement-time curves for the dislocations in the M layers of various All-NL-O configurations in Fig. 15(b). All the curves contain periodic plateaus and rises, a signature of repeated pinning and depinning dislocation motion. The plateaus and rises in the displacement-time curves correspond to the stress rises and drops in the stress-strain curve, respectively. Among all three All-NL-O configurations, the CLS for $d = 0 \text{ nm}$ moves the fastest with the longest rising period in the displacement-time curve, followed by those for $d = 2.5 \text{ nm}$ and $d = 5 \text{ nm}$. This order is consistent with the descending order of the oscillation amplitudes in the stress-strain curves among these three All-NL-O configurations. This suggests that the smaller d leads to the larger stress oscillations and faster CLS.

As a possible explanation for the effect d has on the stress-strain curves and the CLS activities in All-NL-O configurations, we refer to the two interface/dislocation junctions. For $d = 0 \text{ nm}$ in Fig. 17(a), the ledge areas at these sites are nearly anti-symmetric with respect to the x axis. However, for $d = 2.5 \text{ nm}$ and $d = 5 \text{ nm}$, the ledge areas are asymmetric at these two interfaces. Consequently, the stress fields at these sites are anti-symmetric for $d = 0 \text{ nm}$ and asymmetric for $d = 2.5 \text{ nm}$ and $d = 5 \text{ nm}$. The ledge areas and stress fields at the interfaces are able to be explained by Fig. 1(c), where the inserted edge dislocations BC and FE in All-NL-O configuration create the misfit edge dislocations AB, CD, EG and HF at the interfaces. When the confined dislocations BC and FE move, denoted respectively by B'C' and F'E', they drag four misfit screw dislocations, i.e., BB', EE', CC' and FF'. By contrast, the misfit edge dislocations (i.e., AB, CD, EG and HF) remain stationary during loading. Before loading, each of the above misfit edge dislocations creates one ledge at the interface, respectively. Due to the anti-symmetric stress distribution for $d = 0 \text{ nm}$, the dislocations in the M and M' layers remain in their initial position even after thermostat, i.e., at 0 ps in Fig. 16(a). For $d = 2.5 \text{ nm}$ and $d = 5 \text{ nm}$, however, the asymmetric stress distribution together with thermostat shifts the dislocations in M and M' layers along the opposite x directions, respectively. Fig. 16(e) shows an example with $d = 5 \text{ nm}$ at 0 ps.

5. Discussion

The simulation results show that the stress to maintain CLS increases as L decreases, a trend that is anticipated by many analytical models that have come before. Questions on the role of the interface in CLS and whether its contribution produces

another dependence on L , however, arise. At least for the two types of defect-free interfaces studied here, free surface and CTB, we find that the interface resistance can be approximated as an additional contribution that is constant and independent of L . The level of resistance appears to scale with the interface energy. CLS is shown to be harder in the nanofilm than the nanotwinned material, corresponding to the fact that the Nb free surface has an order of magnitude higher energy than the twinned boundary. This resistance may, in fact, be an interface stress, related to changing the interface energy with strain, as proposed previously by Misra et al. (2005), but not necessarily scaling inversely with L .

Apart from the interface, we observe here that CLS in the neighboring layers also influence CLS motion. When CLS is not isolated but the dislocations glide via CLS in concert in every layer the flow stress is substantially reduced. This hints towards the possibility of improving the strength and plasticity of nanolaminate by not only reducing the layer thickness, but tailoring different densities among neighboring layers. Further, a larger separated spacing between the dislocation glide planes in the neighboring layers means more uniform dislocation distribution in nanolaminate, corresponding to a relatively higher strength. Thus, it appears that a good strategy to fabricate stronger nanolaminates would involve homogenizing the dislocations in the neighboring layers.

In our work, MD simulations are performed at a low temperature of 1 K to reduce the influence of thermal fluctuations. However, the main conclusions at such a low temperature still apply to room temperature. In Fig. B.1 in the Appendix, we compare the stress-strain curves of Alt-NL and All-NL-S configurations with $L = 5$ nm at 1 K and 300 K. For both 1 K (low temperature) and 300 K (room temperature), the plateau stress of Alt-NL configuration is much higher than those of All-NL-S configurations. Although All-NL-S configurations with various d only have a slight difference in their plateau stresses at 300 K, such plateau stresses still decrease in the order of $d = 5$ nm, $d = 2.5$ nm and $d = 0$, consistent with the order at 1 K.

Here, our proposed strength-thickness model (i.e., Eq. (11)) only considers a dislocation or dislocations gliding in one plane, whether only in the M layer (Alt-NL configurations or nanofilms) or across many layers along the same direction (All-NL-S configurations with $d = 0$). The model may need to be modified to account for the interactions of dislocations on different planes and/or directions in the neighboring layers, since as we have shown, the effects of these interactions on CLS are strong. Such an extension is planned as future work. Further investigations are also required to test the applicability of our model to cases of forest dislocations in nanolaminated materials. In addition, we focus on CLS between CTBs in a nanotwinned nanolaminate, where the original interfacial dislocations are absent. In practice, interfaces in more common nanolaminates have original interfacial dislocations, such as semi-coherent interfaces in Cu/Ag or Cu/Ni systems (Cui et al., 2019), or incoherent interfaces in Cu/Nb (Wang et al., 2014; Demkowicz et al., 2008) or Zr/Nb systems (Sutton and Balluffi, 1995). Now, the application of our model should be limited in the nanotwinned nanolaminates with coherent interfaces. Investigating the effects of layer thickness and dislocation distribution on the CLS between these semi-coherent or incoherent interfaces in homophase or biphase nanolaminates is recommended for future work, which can also estimate whether our model applies to the other nanolaminates with semi-coherent or incoherent interfaces. Nevertheless, the present study demonstrates that the layer thickness and dislocation distribution in the nanolaminate play important roles in dislocation motion. The insight gained in these dynamic studies can serve as a basis to developing strength theories in the nanolaminates with more complicated interface structures.

6. Conclusions

In this work, we perform atomistic simulations to investigate the effects of layer thickness from 5 nm to 70 nm and dislocation distribution in the adjacent layers on the confined layer slip (CLS) of an edge dislocation between two coherent twin boundaries (CTBs) in Nb/Nb nanolaminates. For reference, the CLS between two free surfaces in nanofilm is also considered. The main findings are below:

- Layer thickness affects dislocation motion. For layer thicknesses finer than 40 nm, CLS is smooth and the dislocation line is nearly straight. For layer thicknesses larger than 40 nm, CLS becomes staggered described by successive pinning and depinning at the two ends of the dislocation and the dislocation line bows out.
- CLS between free surfaces in a Nb nanofilm is initially jerky, due to the alternate pinning and depinning of the line ends, and then becomes smooth after the dislocation line adjusts itself to a stable morphology. Unlike CLS between CTBs, this behavior occurs regardless of the nanolayer thickness.
- The relations calculated from simulation between the critical stress for CLS and nanolayer thickness for the nanolaminate and nanofilm follow the $\ln(L)/L$ scaling law with an additional L -independent resistance. The resistance appears to be positively related to the interface energy.
- Distinct from the classic CLS picture, the motion of a fully threaded dislocation in the Nb nanolaminate was simulated. For the full range of nanolayer thicknesses, CLS is smooth and the dislocation line remains nearly straight. Compared to CLS without concurrent CLS in the neighboring layers, the dependence of the critical stress on nanolayer thickness is substantially reduced. The flow stress associated with the completely threaded dislocation, that is with the simultaneous CLS in all layers sharing the same glide plane and glide direction, is lower than that of the nanofilm.
- In the case of simultaneous CLS in all layers along the same direction but on different parallel planes, we find that the critical stress for CLS and hence flow stress increases as the spacing between their glide planes increases.
- If the sign of the dislocations in the neighboring layers is opposite, CLS motion of every dislocation becomes jerky. The stress-strain response oscillates rather than saturating at a plateau stress and the amplitude of the fluctuations are inversely proportional to their glide plane spacing.

Table A.1

The fitting parameters m and f in the τ_L model (Eq. (9)) for Alt-NL, All-NL-S, and nanofilm configurations. The definitions of Alt-NL and All-NL-S are consistent with those in Fig. 3 and Fig. 5, respectively.

	Alt-NL	All-NL-S	nanofilm
m	0.180	0.0865	0.128
f (MPa · nm)	270.765	1214.104	1816.767

Table A.2

The fitting parameter f in the τ_M model (Eq. (10)) for Alt-NL, All-NL-S, and nanofilm configurations. The definitions of Alt-NL and All-NL-S are consistent with those in Fig. 3 and Fig. 5, respectively.

	Alt-NL	All-NL-S	nanofilm
f (MPa · nm)	1539.967	4548.714	4233.440

Table A.3

The fitting parameters m and f_{int} in the τ_f model (Eq. (11)) for Alt-NL, All-NL-S, and nanofilm configurations. The definitions of Alt-NL and All-NL-S are consistent with those in Fig. 3 and Fig. 5, respectively.

	Alt-NL	All-NL-S	nanofilm
m	0.142	0.00801	0.0120
f_{int} (MPa)	60.7	60.7	88.1

Table A.4

The fitting parameters τ_0 and k in the τ_{HP} model (Eq. (12)) for Alt-NL, All-NL-S, and nanofilm configurations. The definitions of Alt-NL and All-NL-S are consistent with those in Fig. 3 and Fig. 5, respectively.

	Alt-NL	All-NL-S	nanofilm
τ_0 (MPa)	65.7	61.8	68.0
k (MPa · nm ^{0.5})	1096.211	62.603	169.376

CRediT authorship contribution statement

Wu-Rong Jian: Investigation, Formal analysis, Writing – original draft, Writing – review & editing. **Shuzhi Xu:** Conceptualization, Formal analysis, Writing – review & editing. **Yanqing Su:** Investigation, Formal analysis, Writing – review & editing. **Irene J. Beyerlein:** Supervision, Conceptualization, Writing – review & editing.

Declaration of competing interest

The authors declare that they have no known competing financial interests or personal relationships that could have appeared to influence the work reported in this paper.

Acknowledgments

The authors would like to thank Prof. Amit Misra for helpful discussions. W. J. would like to acknowledge support from the Office of Naval Research, United States under Grant No. N000141712810. I. J. B. gratefully acknowledges support from the Office of Naval Research, United States under contract N00014-21-1-2536. Use was made of computational facilities purchased with funds from the National Science Foundation, United States (CNS-1725797) and administered by the Center for Scientific Computing (CSC). The CSC is supported by the California NanoSystems Institute and the Materials Research Science and Engineering Center, United States (MRSEC; NSF DMR 1720256) at UC Santa Barbara.

Appendix A. The fitting parameters for the various analytical CLS models

See Tables A.1–A.4.

Appendix B. The effect of temperature on the shear stress-strain curves of CLS

See Fig. B.1.

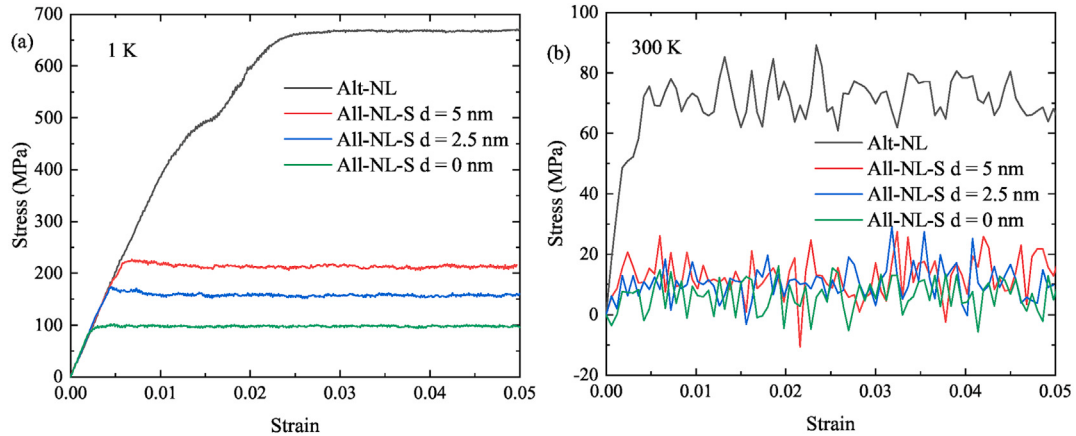


Fig. B.1. Shear stress-strain curves in Alt-NL and All-NL-S configurations with $L = 5$ nm at (a) 1 K and (b) 300 K. Here, d represents the distance the glide planes of the dislocations in the neighboring M and M' layers are separated.

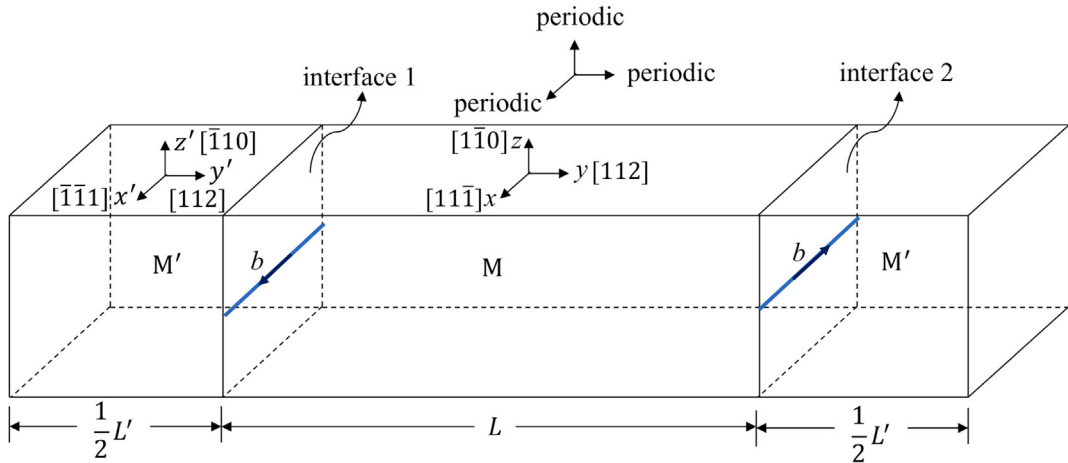


Fig. C.2. Schematic of the atomic configuration used to calculate the interface energy of the Nb nanolaminate where two screw dislocations with the opposite Burgers vectors $\mathbf{b} = (a_0/2)\langle 111 \rangle$ are inserted in the CTBs, respectively. The inserted screw dislocations are denoted by blue solid lines along x direction. The thickness of M and M' layers along y direction are the same, i.e., $L = L' = 5$ nm. (For interpretation of the references to color in this figure legend, the reader is referred to the web version of this article.)

Appendix C. The effect of the inserted screw dislocation on the interface energy of CTB in Nb nanolaminate

To estimate the effect of the inserted screw dislocation on the interface energy of CTB in Nb nanolaminate, we place two screw dislocations with the opposite Burgers vectors $\mathbf{b} = (a_0/2)\langle 111 \rangle$ in the CTBs, respectively (see Fig. C.2). The interface energy of the original CTB is 137.4 mJ/m² and its counterpart with an inserted screw dislocation is 166.3 mJ/m². Thus, a screw dislocation across the x dimension only increases the interface energy by 28.9 mJ/m².

References

- Ackland, G., Thetford, R., 1987. An improved N -body semi-empirical model for body-centred cubic transition metals. *Phil. Mag. A* 56 (1), 15–30.
- Anderson, P., Foecke, T., Hazzledine, P., 1999. Dislocation-based deformation mechanisms in metallic nanolaminates. *MRS Bull.* 24 (2), 27–33.
- Armstrong, R.W., 2014. Hall-petch k dependencies in nanopoly-crystals. *Emerg. Mater. Res.* 3 (6), 246–251.
- Boucher, N., Christian, J., 1972. The influence of pre-strain on deformation twinning in niobium single crystals. *Acta Metall.* 20 (4), 581–591.
- Bufford, D., Wang, H., Zhang, X., 2011. High strength, epitaxial nanotwinned Ag films. *Acta Mater.* 59 (1), 93–101.
- Callisti, M., Polcar, T., 2017. Combined size and texture-dependent deformation and strengthening mechanisms in Zr/Nb nano-multilayers. *Acta Mater.* 124, 247–260.
- Chen, T., Yuan, R., Beyerlein, I.J., Zhou, C., 2020. Predicting the size scaling in strength of nanolayered materials by a discrete slip crystal plasticity model. *Int. J. Plast.* 124, 247–260.
- Cheng, Z., Zhou, H., Lu, Q., Gao, H., Lu, L., 2018. Extra strengthening and work hardening in gradient nanotwinned metals. *Science* 362 (6414), eaau1925.
- Cho, J., Molinari, J.-F., Anciaux, G., 2017. Mobility law of dislocations with several character angles and temperatures in FCC aluminum. *Int. J. Plast.* 90, 66–75.

- Cui, Y., Li, N., Misra, A., 2019. An overview of interface-dominated deformation mechanisms in metallic nanocomposites elucidated using *in situ* straining in a TEM. *J. Mater. Res.* 34 (9), 1469–1478.
- Dang, K., Bamney, D., Bootsma, K., Capolungo, L., Spearot, D.E., 2019. Mobility of dislocations in aluminum: Faceting and asymmetry during nanoscale dislocation shear loop expansion. *Acta Mater.* 168, 426–435.
- Demkowicz, M.J., Beyerlein, I.J., 2020. The effects of nanoscale confinement on the behavior of metal laminates. *Scr. Mater.* 187, 130–136.
- Demkowicz, M.J., Wang, J., Hoagland, R.G., Hirth, J., 2008. Chapter 83 — Interfaces between dissimilar crystalline solids. In: Hirth, J. (Ed.), *Dislocations in Solids*, Vol. 14. pp. 141–207.
- Derlet, P., Gumbsch, P., Hoagland, R., Li, J., McDowell, D., Van Swygenhoven, H., Wang, J., 2009a. Atomistic simulations of dislocations in confined volumes. *MRS Bull.* 34 (3), 184–189.
- Derlet, P., Gumbsch, P., Hoagland, R., Li, J., McDowell, D., Van Swygenhoven, H., Wang, J., 2009b. Atomistic simulations of dislocations in confined volumes. *MRS Bull.* 34 (3), 184–189.
- Embry, J., Hirth, J., 1994. On dislocation storage and the mechanical response of fine scale microstructures. *Acta Metall.* 42 (6), 2051–2056.
- Freund, L., 1987. The stability of a dislocation threading a strained layer on a substrate. *J. Appl. Mech.* 54, 553–557.
- Freund, L., 1990. The driving force for glide of a threading dislocation in a strained epitaxial layer on a substrate. *J. Mech. Phys. Solids* 38 (5), 657–679.
- Frutos, E., Callistri, M., Karlik, M., Polcar, T., 2015. Length-scale-dependent mechanical behaviour of Zr/Nb multilayers as a function of individual layer thickness. *Mater. Sci. Eng. A* 632, 137–146.
- Hall, E., 1951. The deformation and ageing of mild steel: III discussion of results. *Proc. Phys. Soc. Lond. B* 64 (9), 747.
- Hirth, J., Lothe, J., 1982. *Theory of Dislocations*. Wiley, New York.
- Hoagland, R.G., Kurtz, R.J., Henager, Jr., C., 2004. Slip resistance of interfaces and the strength of metallic multilayer composites. *Scr. Mater.* 50 (6), 775–779.
- Huang, S., Beyerlein, I.J., Zhou, C., 2017. Nanograin size effects on the strength of biphasic nanolayered composites. *Sci. Rep.* 7, 11251.
- Jang, D., Li, X., Gao, H., Greer, J.R., 2012. Deformation mechanisms in nanotwinned metal nanopillars. *Nat. Nanotechnol.* 7 (9), 594.
- Jian, W.-R., Su, Y., Xu, S., Ji, W., Beyerlein, I.J., 2021a. Effect of interface structure on dislocation glide behavior in nanolaminates. *J. Mater. Res.* 36, 2802–2815.
- Jian, W., Wang, L., Yao, X., Luo, S., 2018. Tensile and nanoindentation deformation of amorphous/crystalline nanolaminates: Effects of layer thickness and interface type. *Comput. Mater. Sci.* 154, 225–233.
- Jian, W.-R., Xu, S., Beyerlein, I.J., 2021b. On the significance of model design in atomistic calculations of the Peierls stress in Nb. *Comput. Mater. Sci.* 188, 110150.
- Jian, W.-R., Zhang, M., Xu, S., Beyerlein, I.J., 2020. Atomistic simulations of dynamics of an edge dislocation and its interaction with a void in copper: a comparative study. *Modelling Simul. Mater. Sci. Eng.* 28 (4), 045004.
- Kashinath, A., Misra, A., Demkowicz, M., 2013. Stable storage of helium in nanoscale platelets at semicoherent interfaces. *Phys. Rev. Lett.* 110 (8), 086101.
- Lehtinen, A., Granberg, F., Laurson, L., Nordlund, K., Alava, M.J., 2016. Multiscale modeling of dislocation-precipitate interactions in Fe: From molecular dynamics to discrete dislocations. *Phys. Rev. E* 93 (1), 013309.
- Li, N., Demkowicz, M.J., Mara, N.A., 2017. Microstructure evolution and mechanical response of nanolaminate composites irradiated with helium at elevated temperatures. *JOM* 69 (11), 2206–2213.
- Li, N., Nastasi, M., Misra, A., 2012a. Defect structures and hardening mechanisms in high dose helium ion implanted Cu and Cu/Nb multilayer thin films. *Int. J. Plast.* 32, 1–16.
- Li, N., Wang, J., Misra, A., Huang, J.Y., 2012b. Direct observations of confined layer slip in Cu/Nb multilayers. *Microsci. Microanal.* 18 (5), 1155–1162.
- Lin, B., Li, J., Wang, Z., Wang, J., 2020. Dislocation nucleation from Zr–Nb bimetal interfaces cooperating with the dynamic evolution of interfacial dislocations. *Int. J. Plast.* 135, 102830.
- Lu, Y., Kotaka, R., Ligda, J., Cao, B., Yarmolenko, S., Schuster, B., Wei, Q., 2014. The microstructure and mechanical behavior of Mg/Ti multilayers as a function of individual layer thickness. *Acta Mater.* 63, 216–231.
- Martínez, E., Caro, A., Beyerlein, I.J., 2014. Atomistic modeling of defect-induced plasticity in CuNb nanocomposites. *Phys. Rev. B* 90 (5), 054103.
- Martínez, E., Überuaga, B.P., Beyerlein, I.J., 2016. Interaction of small mobile stacking fault tetrahedra with free surfaces, dislocations, and interfaces in Cu and Cu-Nb. *Phys. Rev. B* 93 (5), 054105.
- Misra, A., Demkowicz, M., Wang, J., Hoagland, R., 2008. The multiscale modeling of plastic deformation in metallic nanolayered composites. *JOM* 60 (4), 39–42.
- Misra, A., Hirth, J., Hoagland, R., 2005. Length-scale-dependent deformation mechanisms in incoherent metallic multilayered composites. *Acta Mater.* 53 (18), 4817–4824.
- Misra, A., Hirth, J., Hoagland, R., Embury, J., Kung, H., 2004. Dislocation mechanisms and symmetric slip in rolled nano-scale metallic multilayers. *Acta Mater.* 52 (8), 2387–2394.
- Misra, A., Hirth, J., Kung, H., 2002. Single-dislocation-based strengthening mechanisms in nanoscale metallic multilayers. *Phil. Mag. A* 82 (16), 2935–2951.
- Misra, A., Verdier, M., Lu, Y., Kung, H., Mitchell, T., Nastasi, M., Embury, J., 1998. Structure and mechanical properties of Cu-X (X=Nb, Cr, Ni) nanolayered composites. *Scr. Mater.* 39 (4–5), 555–560.
- Nasim, M., Li, Y., Wen, M., Wen, C., 2020. A review of high-strength nanolaminates and evaluation of their properties. *J. Mater. Sci. Technol.* 50, 215–244.
- Nix, W.D., 1989. Mechanical properties of thin films. *Metall. Trans. A* 20 (11), 2217.
- Orowan, E., 1934. The crystal plasticity. III: about the mechanism of the sliding. *Z. Phys.* 89, 634–659.
- Osetsky, Y.N., Bacon, D.J., 2003. An atomic-level model for studying the dynamics of edge dislocations in metals. *Modelling Simul. Mater. Sci. Eng.* 11 (4), 427.
- Pan, Q., Zhou, H., Lu, Q., Gao, H., Lu, L., 2017. History-independent cyclic response of nanotwinned metals. *Nature* 551 (7679), 214–217.
- Parker, C.A., 1985. Discussion of “enhanced tensile strength for electrodeposited nickel-copper multilayer composites”. *Metall. Trans. A* 16 (9), 1693.
- Pathak, S., Velislavliev, N., Baldwin, J.K., Jain, M., Zheng, S., Mara, N.A., Beyerlein, I.J., 2017. Strong, ductile, and thermally stable bcc-Mg nanolaminates. *Sci. Rep.* 7, 8264.
- Petch, N., 1953. The cleavage strength of polycrystals. *J. Iron Steel Inst.* 174, 25–28.
- Phillips, M., Clemens, B., Nix, W., 2003. A model for dislocation behavior during deformation of Al/Al₃Sc (fcc/L1₂) metallic multilayers. *Acta Mater.* 51 (11), 3157–3170.
- Plimpton, S., 1995. Fast parallel algorithms for short-range molecular dynamics. *J. Comput. Phys.* 117 (1), 1–19.
- Rodney, D., 2007. Activation enthalpy for kink-pair nucleation on dislocations: Comparison between static and dynamic atomic-scale simulations. *Phys. Rev. B* 76 (14), 144108.
- Romero, R.A., Xu, S., Jian, W.-R., Beyerlein, I.J., Ramana, C., 2022. Atomistic simulations of the local slip resistances in four refractory multi-principal element alloys. *Int. J. Plast.* 149, 103157.
- Salehinia, I., Wang, J., Bahr, D., Zbib, H., 2014. Molecular dynamics simulations of plastic deformation in Nb/NbC multilayers. *Int. J. Plast.* 59, 119–132.
- Selimov, A., Xu, S., Chen, Y., McDowell, D.L., 2021. Lattice dislocation induced misfit dislocation evolution in semi-coherent {111} bimetal interfaces. *J. Mater. Res.* 36, 2763–2778.
- Singh, D., Chawla, N., Tang, G., Shen, Y.-L., 2010. Micropillar compression of Al/SiC nanolaminates. *Acta Mater.* 58 (20), 6628–6636.
- Snel, J., Monclús, M., Castillo-Rodríguez, M., Mara, N., Beyerlein, I., Llorca, J., Molina-Aldareguía, J.M., 2017. Deformation mechanism map of Cu/Nb nanoscale metallic multilayers as a function of temperature and layer thickness. *JOM* 69 (11), 2214–2226.
- Stukowski, A., 2009. Visualization and analysis of atomistic simulation data with OVITO—the Open Visualization Tool. *Modelling Simul. Mater. Sci. Eng.* 18 (1), 015012.

- Stukowski, A., Bulatov, V.V., Arsenlis, A., 2012. Automated identification and indexing of dislocations in crystal interfaces. *Modelling Simul. Mater. Sci. Eng.* 20 (8), 085007.
- Subedi, S., Beyerlein, I.J., LeSar, R., Rollett, A.D., 2018. Strength of nanoscale metallic multilayers. *Scr. Mater.* 145, 132–136.
- Sutton, A.P., Balluffi, R.W., 1995. *Interfaces in Crystalline Materials*. Oxford University Press.
- Tench, D., White, J., 1984. Enhanced tensile strength for electrodeposited nickel-copper multilayer composites. *Metall. Trans. A* 15 (11), 2039–2040.
- Turlo, V., Rupert, T.J., 2018. Grain boundary complexions and the strength of nanocrystalline metals: Dislocation emission and propagation. *Acta Mater.* 151, 100–111.
- Wang, M., Beyerlein, I.J., Zhang, J., Han, W.-Z., 2018a. Defect-interface interactions in irradiated Cu/Ag nanocomposites. *Acta Mater.* 160, 211–223.
- Wang, Y., Li, J., Hamza, A.V., Barbee, T.W., 2007. Ductile crystalline-amorphous nanolaminates. *Proc. Natl. Acad. Sci.* 104 (27), 11155–11160.
- Wang, J., Misra, A., 2011. An overview of interface-dominated deformation mechanisms in metallic multilayers. *Curr. Opin. Solid State Mater. Sci.* 15 (1), 20–28.
- Wang, Y.-C., Misra, A., Hoagland, R., 2006. Fatigue properties of nanoscale Cu/Nb multilayers. *Scr. Mater.* 54 (9), 1593–1598.
- Wang, Q., Wang, J., Li, J., Zhang, Z., Mao, S.X., 2018b. Consecutive crystallographic reorientations and superplasticity in body-centered cubic niobium nanowires. *Sci. Adv.* 4 (7), eaas8850.
- Wang, X., Xu, S., Jian, W.-R., Li, X.-G., Su, Y., Beyerlein, I.J., 2021. Generalized stacking fault energies and Peierls stresses in refractory body-centered cubic metals from machine learning-based interatomic potentials. *Comput. Mater. Sci.* 192, 110364.
- Wang, C., Yao, B., Liu, Z., Kong, X., Legu, D., Zhang, R., Deng, Y., 2020. Effects of solutes on dislocation nucleation and interface sliding of bimetal semi-coherent interface. *Int. J. Plast.* 131, 102725.
- Wang, J., Zhang, R., Zhou, C., Beyerlein, I.J., Misra, A., 2014. Interface dislocation patterns and dislocation nucleation in face-centered-cubic and body-centered-cubic bicrystal interfaces. *Int. J. Plast.* 53, 40–55.
- Wang, J., Zhou, Q., Shao, S., Misra, A., 2017. Strength and plasticity of nanolaminated materials. *Mater. Res. Lett.* 5 (1), 1–19.
- Xie, Z., Jian, W.-R., Wang, Z., Zhang, X., Yao, X., 2020. Layer thickness effects on the strengthening and toughening mechanisms in metallic glass-graphene nanolaminates. *Comput. Mater. Sci.* 177, 109536.
- Xu, S., Cheng, J.Y., Li, Z., Mara, N.A., Beyerlein, I.J., 2022. Phase-field modeling of the interactions between an edge dislocation and an array of obstacles. *Comput. Methods Appl. Mech. Engrg.* 389, 114426.
- Xu, S., Li, Y., Chen, Y., 2020a. Si/Ge (111) semicoherent interfaces: Responses to an in-plane shear and interactions with lattice dislocations. *Phys. Status Solidi (B)* 257, 2000274.
- Xu, S., Mianroodi, J.R., Hunter, A., Svendsen, B., Beyerlein, I.J., 2020b. Comparative modeling of the disregistry and Peierls stress for dissociated edge and screw dislocations in Al. *Int. J. Plast.* 129, 102689.
- Xu, S., Smith, L., Mianroodi, J.R., Hunter, A., Svendsen, B., Beyerlein, I.J., 2019a. A comparison of different continuum approaches in modeling mixed-type dislocations in Al. *Modelling Simul. Mater. Sci. Eng.* 27 (7), 074004.
- Xu, S., Su, Y., Beyerlein, I.J., 2019b. Modeling dislocations with arbitrary character angle in face-centered cubic transition metals using the phase-field dislocation dynamics method with full anisotropic elasticity. *Mech. Mater.* 139, 103200.
- Xu, S., Su, Y., Jian, W.-R., Beyerlein, I.J., 2021. Local slip resistances in equal-molar MoNbTi multi-principal element alloy. *Acta Mater.* 202, 68–79.
- Xu, S., Su, Y., Smith, L.T.W., Beyerlein, I.J., 2020c. Frank-read source operation in six body-centered cubic refractory metals. *J. Mech. Phys. Solids* 141, 104017.
- Xu, S., Xiong, L., Chen, Y., McDowell, D.L., 2016a. An analysis of key characteristics of the Frank-Read source process in FCC metals. *J. Mech. Phys. Solids* 96, 460–476.
- Xu, S., Xiong, L., Chen, Y., McDowell, D.L., 2016b. Sequential slip transfer of mixed-character dislocations across $\Sigma 3$ coherent twin boundary in FCC metals: a concurrent atomistic-continuum study. *Npj Comput. Mater.* 2, 15016.
- Xu, S., Xiong, L., Chen, Y., McDowell, D.L., 2017. Comparing EAM potentials to model slip transfer of sequential mixed character dislocations across two symmetric tilt grain boundaries in Ni. *JOM* 69 (5), 814–821.
- Xu, J., Xu, S., Beyerlein, I.J., 2019c. Atomistic simulations of dipole tilt wall stability in thin films. *Thin Solid Films* 689, 137457.
- Yang, W., Beyerlein, I.J., Jin, Q., Ge, H., Xiong, T., Yang, L., Pang, J., Zhou, Y., Shao, X., Zhang, B., et al., 2019. Strength and ductility of bulk Cu/Nb nanolaminates exposed to extremely high temperatures. *Scr. Mater.* 166, 73–77.
- Zhang, X., Fu, E., Li, N., Misra, A., Wang, Y.-Q., Shao, L., Wang, H., 2012. Design of radiation tolerant nanostructured metallic multilayers. *J. Eng. Mater. Technol.* 134 (4).
- Zhang, L., Martinez, E., Caro, A., Liu, X.-Y., Demkowicz, M.J., 2013. Liquid-phase thermodynamics and structures in the Cu-Nb binary system. *Modelling Simul. Mater. Sci. Eng.* 21 (2), 025005.
- Zheng, S., Beyerlein, I., Wang, J., Carpenter, J., Han, W., Mara, N.A., 2012. Deformation twinning mechanisms from bimetal interfaces as revealed by in situ straining in the TEM. *Acta Mater.* 60 (16), 5858–5866.